Journal of Colloid and Interface Science 621 (2022) 416–430

Contents lists available at ScienceDirect

Journal of Colloid and Interface Science

journal homepage: www.elsevier.com/locate/jcis

Silver boosts ultra-long cycle life for metal sulfide lithium-ion battery anodes: Taking $AgSbS_2$ nanowires as an example

Sheng-Feng Ho, Yi-Chun Yang, Hsing-Yu Tuan *

Department of Chemical Engineering, National Tsing Hua University, Hsinchu 30013, Taiwan

GRAPHICAL ABSTRACT

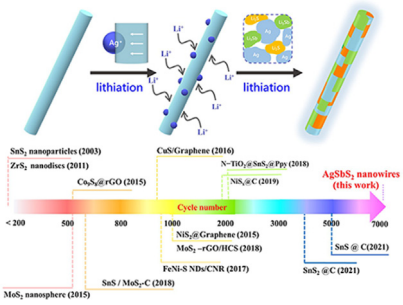

ARTICLE INFO

Article history:
Received 9 February 2022
Revised 23 March 2022
Accepted 4 April 2022
Available online 09 April 2022

Keywords:
Silver
Metal sulfide
Lithium ion
Battery
Nanowire

ABSTRACT

Metal sulfide, being a high-capacity anode material, is a promising anode material for rechargeable lithium-ion batteries (LIBs). However, most research efforts have focused on improving their low cycling performance due to multiple combined factors, including low conductivity, huge volume changes, multi-step conversion/alloying reactions, and redox shuttling effect, during the cycling process. Here, we report that by using $AgSbS_2$ nanowires as LIB anode materials, a record-breaking long cycle life metal sulfide anode has been achieved through the silver synergistic electrochemical performance effect. We found that while the $AgSbS_2$ nanowire anode is cycled, Ag precipitated out to form a nanocrystal tightly connected with Sb and S and plays a key role in highly-reversible electrochemical performance. Ag can effectively enhance the electrode conductivity, increase ion diffusion rate, serve a diluent huge volume changes during conversion-alloying reactions, improve the absorbability and catalytic ability towards LiPSs to reduce shutting effect of sulfur, and enhanced Li^+ adsorption. As a result, $AgSbS_2$ nanowire anodes maintain 90% capacity retention over 5000 and 7000 cycles at the current densities of 500 mA g^{-1} and 2000 mA g^{-1}, respectively, whereas the capacities of Sb_2S_3 nanowire and Sb_2S_3/C nanowire anodes drop rapidly within 10 cycles. The ultra-stable cycle life is superior to the state-of-the-art metal sulfide anodes. Finally, using $AgSbS_2$ nanowires as the anode combined with the cathode $LiNi_5Co_3Mn_2$, a full battery after 480 cycles was assembled to verify that its stability (high retention rate of 99.5%) can be used in the current commercial battery architecture. This work solves multiple problems related to shuttling effects and complex reactions of metal sulfide anodes, and provides important progress for the future development of metal sulfide anodes for LIBs.

* Corresponding author.
E-mail address: hytuan@che.nthu.edu.tw (H.-Y. Tuan).

https://doi.org/10.1016/j.jcis.2022.04.020
0021-9797/

1. Introduction

With the increasing demand for electric vehicles and electronic products, lithium-ion batteries (LIBs) have become the most important electrical energy storage devices [1]. LIBs have the advantages of high energy density [2–5], good rate performance [6,7], long cycle life [8,9], and high output voltage [10]. As for the anode material, the theoretical capacity of the commercial graphite anode is only about 372 mA h g^{-1}, which limits the further development of its energy density [11]. Other potential LIB anode materials, such as alloyed elements (*e.g.*, Sb, Sn, and Si) [12], metal oxide materials (*e.g.*, SnO_2, SiO, Fe_2O_3,) [13,14], metal chalcogenides (*e.g.*, Cu_xS, Ni_xS, SnS_2, MoS_2, and Sb_2S_3) [15] have been studied as anode alternatives. These materials deliver a capacity of>500 mA h g^{-1} through the conversion and/or alloying reactions with Li^+. However, poor electrode stability during cycling restricts their commercialization possibility.

Metal sulfides have high LIB theoretical capacities (>400 mA h g^{-1}), unique electrochemical characteristics, and various structural features such as nanowires, and are used in multiple fields [16–19]. For example, antimony sulfide (Sb_2S_3) is a model system because it has a working potential of approximately 1 V vs. Li^+/Li, far away from the potential for forming lithium dendrites, making it a safer anode electrode material for fast charging applications [20]. Based on the transfer of $M_xS_y + 2yLi^+ + 2ye^- \rightarrow xM + yLi_2S$, the metal sulfides not only undergo the conversion reaction between Li^+ and M_xS_y, but also proceeds the alloying reactions between the remaining metal and Li^+. In addition, sulfur has abundant reserves on the earth and the cost is extremely low. Compared with in metal oxides, metal sulfides have weak M−S bonds, thus leading to faster metal sulfide kinetics and more stable mechanical properties during the conversion reaction [21–25]. However, poor conductivity and large volume changes during the cycle reduce cycle stability and rate capability, further limiting their practical applications [26–31]. In addition, sulfide is easily dissolved in the electrolyte, causing a shuttle effect to affect cycle life achieving less than 500 cycles and leading to low electrode conductivity and electrode powdering [32–34]. The widely used method is to improve the electronic conductivity and mechanical stability of the electrode materials through the strategy of using nanomaterials as electrodes or carbon coating, thereby improving the cycle stability and solving the problems of sulfide-based electrodes. For example, one-dimensional (1D) nanostructures, such as nanowires[35–37], nanobelts [38], nanofibers [39], nanorods [40–42], nanotubes [43], can provide abundant electrochemical active sites due to high aspect ratio and good mechanical strength, the characteristics of high surface area, large electrolyte–electrode contact area and reduced charging/discharging time so as to provide excellent electron transmission paths. The hybridization of nanosized metal sulfides with carbon materials such as graphene [44], carbon nanotubes, and porous carbon is an effective way to avoid the above-mentioned problems [45,46]. However, carbon-based reactions require complex, high-temperature, multi-step procedures, and the carbon content is difficult to control, often accounting for a large proportion of composites. Metal sulfide anodes still requires the focus of the development for extending the cycle stability to meet the needs of durable electronic devices.

Recently, the synergy between the metal elements in the ternary metal sulfide materials and the new chemical reactions between the elements and lithium ions have attracted intense attention [47]. For example, the Cu in $CuSbS_2$ electrode plays a critical role in the conversion reaction and the subsequent alloying reaction of Sb and Li^+. Cu is an inert element to Li^+, but it provides high electrical conductivity (6×10^5 S m^{-1}) to promote charge transfer during electrochemical reactions. Moreover, Cu produce a "dilution effect" to keep the alloying area small or prevent/limit the agglomeration of alloyed particles [48,49]. Yadav *et al.* reported that the addition Cu to binary antimony sulfide (Sb_2S_3) to form ternary copper antimony sulfide ($CuSbS_2$) that can increase conductivity and decrease capacity loss [50]. However, despite improvements by Cu, $CuSbS_2$ electrode still requires the addition of reduced graphene oxide (rGO) to form $CuSbS_2$-rGO composite material, and only extended a cycle life to 1000 cycles.

Ag has a larger ion radius and higher electron affinity and conductivity than Cu, but whether there is a positive improvement in LIB anodes has rarely been studied. Here, we report by using $AgSbS_2$ nanowires as an anode that is capable to be cycled up to 7000 times for LIBs, which is superior to the state-of-the-art metal sulfide anodes. $AgSbS_2$ nanowires provide electrochemically active sites and excellent electron transport paths. Fig. 1 shows the difference between using $AgSbS_2$ and Sb_2S_3 nanowire anode materials. We show that Ag has multiple functions to improve the cycle life of metal sulfides in LIBs, reducing the electrode resistivity, acting as a diluent to reduce the huge volume change during cycling, constraining the shuttling effect of sulfur, and enhancing Li^+ adsorption to improve the cycle performance of metal sulfides in LIBs. On the contrary, the cycle performance of Sb_2S_3 is poor due to active material pulverization, serious volume expansion and obvious shuttling effect. Moreover, the full cell displays a reversible capacity of 400 mA h g^{-1} after 480 cycles at 500 mA g^{-1} (high retention rate of 99.5%) was fabricated with $LiNi_5Co_3Mn_2$ cathode and $AgSbS_2$ anode. This work does not need to be coated with carbon but simply uses silver to achieve ultra-stable cycle life, which will further promote the use of metal sulfides in LIBs.

2. Experimental section

2.1. Chemicals

All materials were used as received without purification. Silver nitrate (>99.5%) was purchased from Sigma-Aldrich. Antimony chloride (>99.5%) was purchased from Alfa-Aesar. Thioacetamide (>99.5%) was purchased from Sigma-Aldrich. Hexadecyltrimethylammonium bromide (>99.9%) was purchased from Alfa-Aesar. Na_2S 9 H_2O (>99.5 %) and ethylene glycol (extra pure) were purchased from Sigma-Aldrich. Li metal foil, membrane, copper foil (0.01 mm), electrolyte (1 M $LiPF_6$ in ethyl carbonate/dimethyl carbonate (EC/DMC) (1:1 vol%), adding 10 wt% additional fluoroethylene carbonate (FEC), super P carbon black, coin-type cell (CR2032), were obtained from shining energy.

2.2. Preparation of $AgSbS_2$ nanowires

The synthesis of $AgSbS_2$ nanowires were synthesized by a solvothermal reaction. We first dissolved a certain amount of CTAB in 30 ml of ethylene glycol with magnetic stirring at room temperature for 30 min. Next, 0.1 mmol silver nitrate, 0.1 mmol antimony chloride, and 0.2 mmol thioacetamide were added simultaneously to the solution and mixed for another 15 min. The color of the solution will change from white to light orange after all materials were well-mixed. Then, the resulting solution is transferred to a Teflon-lined stainless-steel autoclave and the temperature is remained the same at 180 °C for 12 h. After that, the autoclave is cooled to room temperature, and the precipitates were collected by centrifugation for several times with ethanol. Finally, the $AgSbS_2$ nanowires were synthesized for further analysis.

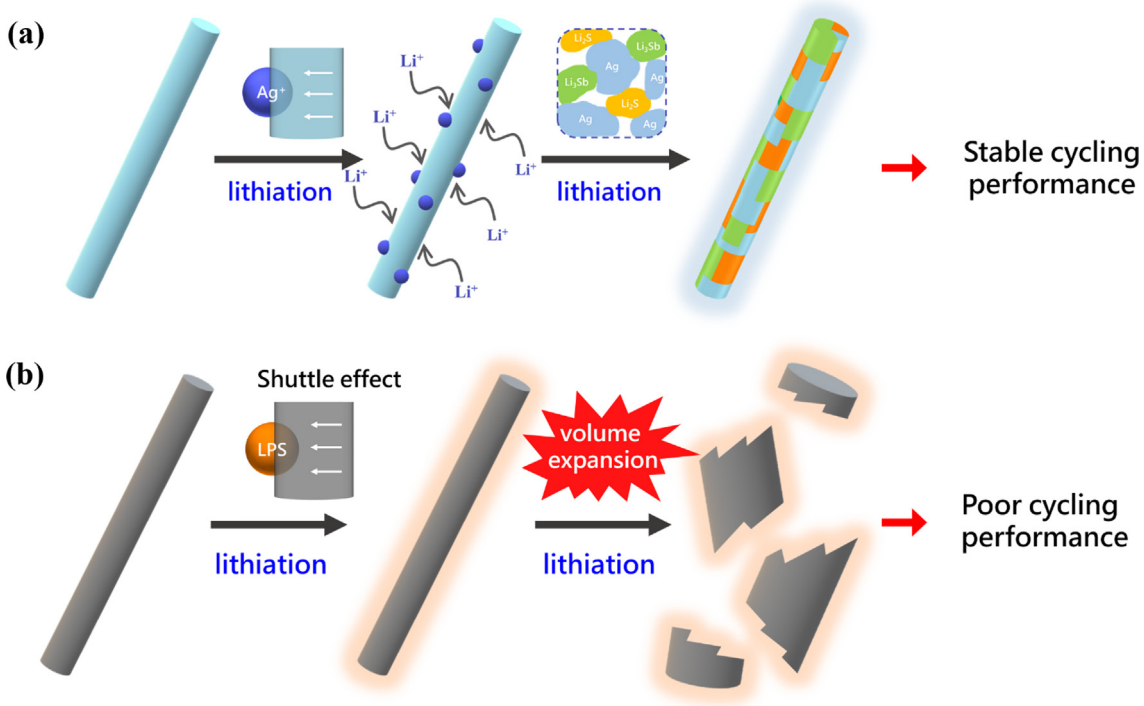

Fig. 1. Schematic diagram showing the different changes of $AbSbS_2$ and Sb_2S_3 nanowire anodes during lithiation and resulting in different cycle performance results.

2.3. Preparation of Sb_2S_3 nanowires

Sb_2S_3 nanowires were prepared via a solvothermal process. First, 2 mmol $SbCl_3$ and 4 mmol $Na_2S{\cdot}9\ H_2O$ were dissolved in 25 ml ethylene glycol to form solution A and B, respectively. Then, solution A was added slowly in droplet into solution B under vigorous stirring. The color of the solution will turn orange, indicating the intermediate phase formed during the process. The resulting mixture was loaded into a Teflon-lined stainless-steel autoclave, and the temperature was maintained at 200 °C for 10 h. The resulting products were centrifuged and washed with ethanol for several times, and Sb_2S_3 nanowires were obtained after drying at 40 °C for 4 h.

2.4. Synthesis of Sb_2S_3/C composites

Sb_2S_3/C composites was synthesized via a ball-milling process. Typically, 100 mg of the as-synthesized Sb_2S_3 and 25 mg of super P was put into zirconia jars. Then, the raw materials were ball milled in a planetary ball milling machine for 12 h at 400 rpm, and the ball to powder weight ratio was set to 10: 1. Finally, the black powder was obtained without any purification for further use.

2.5. Electrochemical characterization

The $AgSbS_2$ nanowires electrodes were fabricated by mixing the active material ($AgSbS_2$ nanowires, 70 wt%), super P (20 wt%), and polyacrylic acid (PAA, 10 wt%) in 1 ml anhydrous ethanol to form a homogeneous slurry, which continued to be casted on the copper foil. Before a coin cell assembly, the electrode is dried at 80 °C under argon gas for 90 min to remove residual water and excess solvent. Then, the electrode is shaped to a circle with 12 mm diameter and densely pressed with a rolling machine. All coin cells were assembled in an argon-filled glove box. We used 1 M $LiPF_6$ dissolved in ethyl carbonate/dimethyl carbonate (EC/DMC (1:1 vol %)), with 10 wt% additional fluoroethylene carbonate (FEC) as the electrolyte solution. Finally, electrochemical performance of $AgSbS_2$ nanowires is tested using Neware battery test systems.

2.6. Characterization

The structure of the product and *ex-situ* XRD test are characterized by X-ray diffraction (XRD) pattern (Bruker, D8). The surface morphologies of the product were investigated by means of scanning electron microscopy (SEM), and the HITACHI-S4800 field emission SEM with 10–15 kV accelerating voltage and 8 mm working distance recorded the $AgSbS_2$ nanowires. Moreover, energy dispersive X-ray spectroscopy (EDS) and high-resolution transmission electron microscopy (HRTEM) also helped to observe the product's composition and structure, and were operated under 200 kV. X-ray photoelectron spectroscopy (XPS) was conducted by using ULVAC-PHI. Raman spectra was obtained by LABRAM HR 800 UV via green light.

2.7. Computational section

The density functional theory calculations were performed by the Vienna Ab initio Simulation Package (VASP) code [51]. The electron ion interaction was described with the projector augmented wave method [52]. In the calculations, the electron exchange and correlation energy were treated within the generalized gradient approximation in the Perdew–Burke–Ernzerhof formalism. A plane-wave cutoff energy basis was set as 450 eV. The Sb_2S_3(100) surface, Ag/Sb heterojunction, Ag/Sb/S heterojunction, Ag/S heterojunction, Sb/S heterojunction were used to study the adsorption properties of Li atom, Li_2S, Li_2S_2, Li_2S_4, Li_2S_6, and Li_2S_8. All surface were simulated with slab model, and the thickness of vacuum was set to 18 Å to eliminate the interaction between slabs. The vdW interaction corrections were included to in all calculations. The force and energy convergence criteria were set as 0.01 eV $Å^{-1}$ and 10^{-4} eV, respectively. The adsorption energies of

molecule (or atom) on the surface (or heterojunction) were calculated as below:

$$E_{ad} = E(mol/atom + surf/hetero) - E(surf/hetero) - E(mol/atom)$$

where E(mol/atom + surf/hetero), E(surf/hetero) and E(mol/atom) are the total energies of the surface (or heterojunction) with molecule (or atom), surface (or heterojunction) and the molecule (or atom), respectively.

2.8. Lithium-ion full cell of $AgSbS_2$ // $Li(Ni_{0.5}Co_{0.3}Mn_{0.2})O_2$

For the lithium-ion full cell assembly, the mass ratio of $AgSbS_2$ nanowires to $Li(Ni_{0.5}Co_{0.3}Mn_{0.2})O_2$ was about 0.6 based on the areal capacity (mA h cm^{-2}) at 500 mA g^{-1}. The electrolyte was same with the $AgSbS_2$ half-cell by using 1 M $LiPF_6$ in (EC/DMC (1:1 vol%)), with 10 wt% additional fluoroethylene carbonate (FEC). The working window of the full cell was ranged from 0.5 V ~ 4.1 V.

3. Results and discussion

The hydrothermal synthesis procedure for the $AgSbS_2$ nanowires is schematically illustrated in Fig. 2a. Initially, $AgNO_3$ and $SbCl_3$ are dissolved in ethylene glycol containing CTAB. The addition of a surfactant (CTAB) can effectively adjust the morphology and structure of nanomaterials through coordination or charge effects [53]. Then, C_2H_5NS is added to form an orange intermediate under stirring. Finally, the black precipitate is obtained at 180 °C for 12 h. The detailed morphologies and microstructures of the samples were investigated by scanning electron microscope (SEM) and transmission electron microscope (TEM). Fig. 2b and c show the SEM images of $AgSbS_2$ nanowires. The low-magnification image shows that the nanowires are distributed uniformly, and a smooth and clean surface. The high-magnification image shows that the $AgSbS_2$ nanowires with an average diameter of 10–40 nm. Fig. 2d shows the TEM image of $AgSbS_2$ nanowires with straight morphology. The high-resolution TEM (HRTEM) image of $AgSbS_2$ confirms the lattice spacing of 0.288 nm, indexed to the (100) plane of which can be designated as the (200) plane of the $AgSbS_2$ phase (Fig. 2e and f). The indexed (111), (200) and (220) planes in the selected area electron diffraction (SAED) pattern are in accordance with the XRD pattern of $AgSbS_2$ (Fig. 2g). HRTEM image and SAED pattern illustrate the single crystal nature of $AgSbS_2$. Energy dispersive X-ray spectroscopy (EDS) further shows that Ag, Sb and S are uniformly distributed in the compound (Fig. 2h-k).

The crystal structure of the synthesized $AgSbS_2$ was explored by X-ray diffraction (XRD) (Fig. 3a). Diffraction peaks can be observed at 27.31°, 31.64°, 45.35° and 53.75°, corresponding to the (111), (200), (221), and (311) planes, respectively. All diffraction peaks can be well assigned to the cubic crystal phase $AgSbS_2$ (JCPDS 98–041-2240) with the *Fm*-3 m (22) space group, indicating the as-obtained product is highly pure. The elemental analysis of the surfaces of the as-prepared $AgSbS_2$ nanowire was performed using X-ray photoelectron spectroscopy (XPS) to detect Ag, Sb and S elements (Fig. 3b). The high-resolution Ag 3d spectrum shows two peaks located at around 374 and 368 eV, corresponding to the bands of Ag $3d_{2/3}$ and Ag $3d_{5/2}$, respectively (Fig. 3c). In the high-resolution Sb 3d spectrum, two peaks at about 540.7 eV and 531.5 eV belong to Sb $3d_{2/3}$ and Sb $3d_{5/2}$, respectively, as shown in Fig. 3d. The Sb 4d spectrum is also analyzed, which can be deconvoluted into two peaks at 34.5 eV and 33 eV, corresponding to the bands of Sb $4d_{2/3}$ and Sb $4d_{2/5}$, respectively (Fig. 3e). In addition, S 2p spectrum showed two typical peaks at 163 eV and 161.5 eV, belonging to S $2p_{1/2}$ and S $2p_{2/3}$ (Fig. 3f) [54]. Moreover, Brunauer–Emmett–Teller (BET) test using continuous-flow gas(N2) adsorption was conducted as shown in Figure S1. The surface area of $AgSbS_2$, Sb_2S_3, and Sb_2S_3 / C was examined to be 1.9 m^2/ g, 4 m^2/ g, and 2.3 m^2/ g, respectively, which confirmed that all obtained material were non-porous. In addition, duo to the surfactant plays an important role in regulating the morphology of nanomaterials, different kinds of surfactant were investigated to prepare $AgSbS_2$ nanowires, such as cationic surfactants (CTAB) and non-ionic surfactants (PVP, Oleylamine). Figure S2 shows the influence of different surfactants on the morphology of $AgSbS_2$ material. The uniform $AgSbS_2$ nanowires with an average diameter of 10–40 nm can be synthesized using CTAB as a surfactant (Figure S2a). Figures S2b and c show $AgSbS_2$ nanowires synthesized by PVP with MW = 40000 and MW = 55000, respectively. It can be found that the $AgSbS_2$ nanowires synthesized by PVP are thick and short with uneven dimensions, indicating that PVP is unfavorable to the stability of the structure. As shown in Figure S2d, it can be observed that the morphology of $AgSbS_2$ synthesized by oleylamine is nanowires, but there are many faceted nanocrystals. Therefore, CTAB is used in the synthesis of $AgSbS_2$ to facilitate the formation of uniform nanowires because the good dispersibility of CTAB in the solution and excellent coordination properties with the anion as a cationic surfactant. In addition, the crystallinity, purity and morphology of the product can be affected by the reaction time. As shown in Figure S3, when time of hydrothermal treatment increases, the faceted nanocrystals gradually decrease. In order to obtain high-quality of single crystal $AgSbS_2$ nanowires, the control of reaction time is important.

The lithium storage performance of $AgSbS_2$ nanowires was shown in Fig. 4; the cycle performances of $AgSbS_2$ nanowires in different electrolyte were shown in Figure S4. As a control sample, Sb_2S_3 and Sb_2S_3/C nanowires were prepared by a simple hydrothermal synthesis [55] (Figures S4 and 5). Fig. 4a presents that the $AgSbS_2$ nanowires deliver a high discharge capacity of 904.5 mA h g^{-1} with an initial Coulombic efficiency of 62.3%. The capacity loss of 37.7% is mainly due to the irreversible formation of SEI films. Coulombic efficiency for each cycle is another important role for cycle stability. For 500 cycles, the Coulombic efficiency for $AgSbS_2$ exceeds 99.3%. Additionally, high Coulombic efficiency can be achieved through the formation of the stability SEI layer after the first cycle. The galvanostatic discharge profiles of the 10th and 50th cycle are shown in Fig. 4b and c. The high plateau profile and the second plateau are corresponded to $AgSbS_2 + 4e^- + 4Li^+ \rightarrow Ag + 2Li_2S + Sb$ and $Sb + 3Li^+ + 3e^- \rightarrow Li_3Sb$, respectively. For the 10th cycle, the plateau of $AgSbS_2$ exhibits longer because Ag are involved. The discharge special capacity of Sb_2S_3 exhibit almost no capacity after full activation with 50th cycle due to huge volume expansion and poor ion/electron conductivity. On the other hand, although the cycle stability of Sb_2S_3 nanowire is improved through the strategy of carbon coating, Sb_2S_3/C nanowires exhibits only discharge capacity of 128.1 mA h g^{-1} after 500 cycles at 500 mA h g^{-1}. It is worth noting that $AgSbS_2$ nanowires exhibit an excellent rate capability at different current densities from 0.05 to 4 A g^{-1}, as shown in Fig. 4d. It delivers reversible capacities of 517, 468.9, 419.8, 385.3, 350.1, and 265.1 mA h g^{-1} at various current rates of 0.05, 0.1, 0.25, 0.5, 1, and 2 A g^{-1}, respectively. When the rate increases to 4 A g^{-1}, a reversible capacity of 190.3 mA h g^{-1} can still be obtained, showing excellent high rate performance. After that, the capacity quickly recovers to 522.1 mA h g^{-1} when the current rate returns back to 0.05 A g^{-1}, exhibiting a good retention capacity. Compared with the value before the high-rate cycling process, this value only has a loss of 2.92%. The corresponding charge/discharge curves at different rates are shown in Figure S7. For comparison, Sb_2S_3 nanowires deliver 450, 382, 310, 256, 251, 199 and 138.5 mA h g^{-1} at the same current rate protocol as $AgSbS_2$ nanowires. The rate capabil-

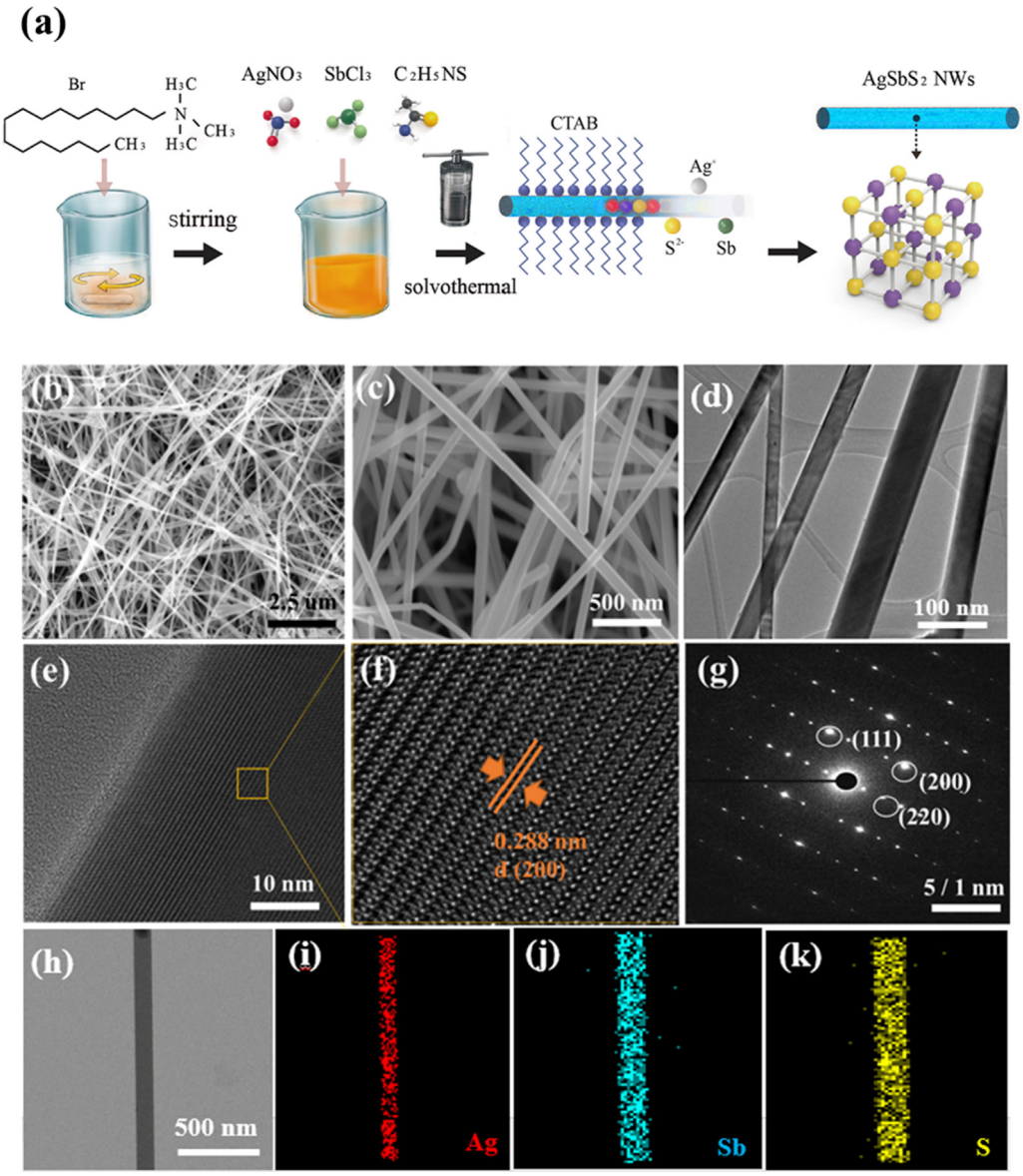

Fig. 2. (a) Schematic illustration of $AgSbS_2$ nanowires via hydrothermal synthesis. (b, c) SEM images, (d) TEM image, (e, f) HRTEM images and (g) SAED pattern of $AgSbS_2$ nanowires. (h-k) EDS mapping images of Ag, S and Sb in $AgSbS_2$ nanowires.

ity of Sb_2S_3 as well as Sb_2S_3/C nanowires is unsatisfactory, with a rapid capacity decay. As shown in Fig. 4e, $AgSbS_2$ anodes maintain a high reversible capacity of 185 mA h g^{-1} after 5000 cycles at 500 mA h g^{-1}, with an average Coulombic efficiency of 99.3%, indicating once a stable SEI is formed, $AgSbS_2$ exhibit extraordinary stable cycle life. Significantly, the $AgSbS_2$ anode cycled at a rate of 500 mA g^{-1} retains 98% of its 100th capacity after 2000 cycles and 96% of its 100th capacity after 5000 cycles. Fig. 4f shows the charge–discharge voltage plateaus are still very obvious in 5000 cycles, indicating its excellent reversibility. In order to further explore the effect of Ag on $AgSbS_2$ anodes, the cycling test is conducted at a high current density of 2000 mA g^{-1} and the corresponding charge–discharge curves, as shown in Fig. 4g and h. It maintains reversible capacity of 185.3 mA h g^{-1} at 2 A g^{-1} with each cycle's average Coulombic efficiency is approximately 99%. Significantly, the $AgSbS_2$ anode cycled at a rate of 2 A g^{-1} retains 90.6% of its 100th capacity after 7000 cycles. Due to the large volume changes and shuttle effect, the cycle performance of metal sulfide is poor for LIBs, resulting in hindering the further development and application in rechargeable LIBs. We also compare the cycle life with the previous reports based on S-based electrode materials (Fig. 4i). It's worth noting that $AgSbS_2$ nanowires have the best cycle stability performance without carbon-coating for lithium-ion anodes with a cycle number of $AgSbS_2$ lives up to 7000 cycles at 2 A g^{-1}. It is found that the cycle number of S based anodes designed by nanomaterial or carbon coating is increased to 5000 cycles at most. Mukaibo *et al.* reported that SnS_2 particles with a small particle size have higher reversible capacity and cycle stability than large particle size [56], but the cycle number still did not exceed 100. It has been reported that through the nanostructure design and composite materials, nano-sized electrode materials have significant advantages, including short Li^+ diffusion paths, large electrode/electrolyte contact areas, and strain adjustment, resulting in higher rate performance and better cycle life. Recently, it is mostly reported that the use of graphene or graphene derivatives can solve these problems and improve the electrochemical performance of LIBs [57–59]. This can be attributed to the characteristics of graphene: two-dimensional conductive network, large

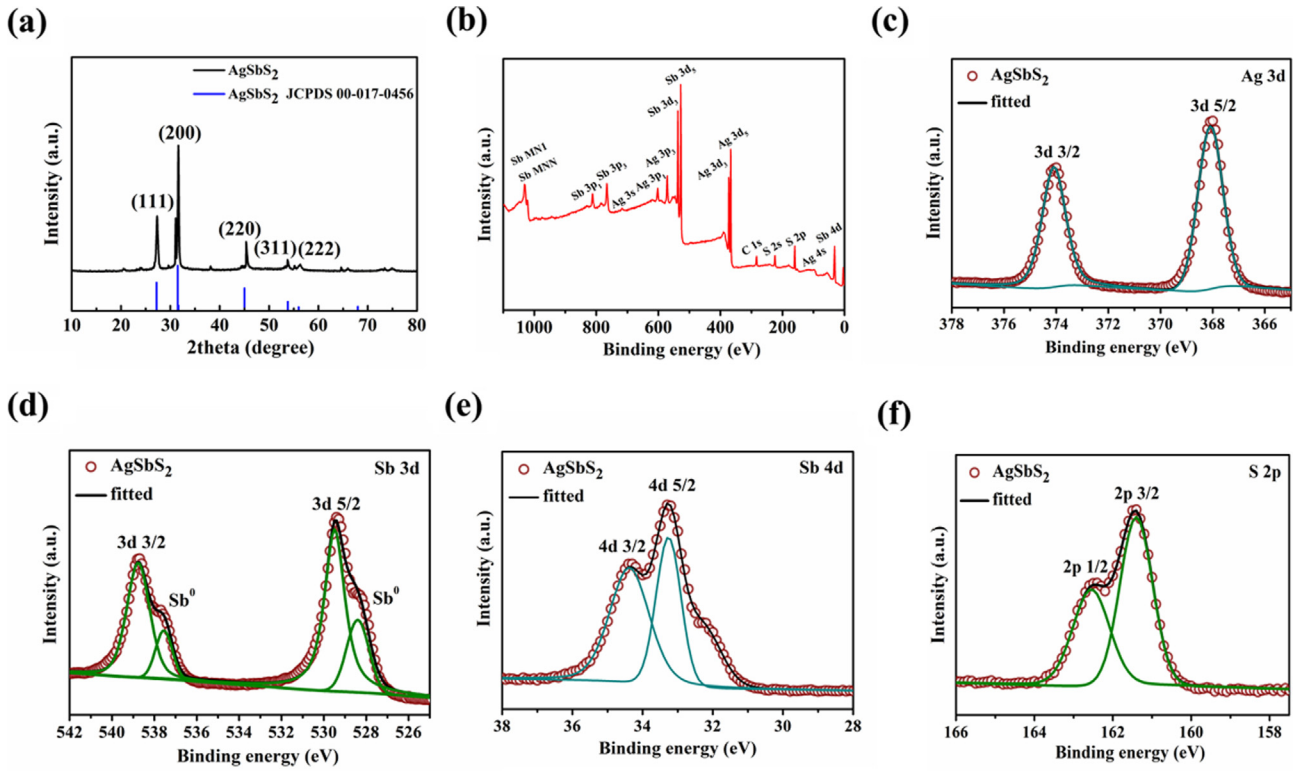

Fig. 3. (a) XRD pattern and High-resolution XPS spectra of (b) survey XPS spectrum, (c) Ag 3d, (d) Sb 4d, (e) S 2p, and (f) Sb 3d for $AgSbS_2$ nanowires.

specific surface area and good physical and chemical stability. In addition to these characteristics, their porous structure can effectively promote the diffusion of electrolyte ions, such as Co_9S_8@rGO (2015) [60], CuS/Graphene (2016) [61], NiS_2@Graphene (2015) [62] and MoS_2 -rGO/HCS (2018) [63] and so on. Moreover, due to excellent electrical conductivity and high stability, the lithium storage performance of the metal composite materials of sulfide and carbon can be improved, such as FeNi-S NDs/CNR (2017) [64], SnS/MoS_2-C (2018) [65], N – TiO_2@SnS_2@Ppy (2018) [66], NiSx@C (2019) [67], SnS_2 @C (2021) [68], etc. Therefore, $AgSbS_2$ nanowires have obvious advantages under long-term cycling, indicating that Ag can improve the cycling performance and rate performance of metal sulfides used in LIBs.

A kinetic analysis was performed for evaluating the capacitive contribution to Li^+ storage based on CV scans ranging from 0.2 to 1 mV s^{-1}. The CV curves show a similar shape with obvious redox peaks, meaning that lithium-ion storage has high reversibility and fast kinetics (Fig. 5a). The relationship between peak current (i) and scan rate (v) can be written as the following equation:

$$i = av^b \tag{1}$$

Where a and b are constants, the b-value represents the type of charge-storage mechanism. Notably, the value of b is 0.5 represents the diffusion-controlled process, and 1.0 represents the capacitive-controlled process. As shown in Fig. 5b, the b values of oxidation and reduction peaks are 0.9052 and 0.9931, respectively, indicating that the Li^+-storage mechanism of $AgSbS_2$ nanowires involves pseudo-capacitive effect. Furthermore, the pseudo-capacitance contribution can be further quantified by the following formula:

$$i(v) = k_1 v + k_2 v^{1/2} \tag{2}$$

The total charge storage is the sum of the contributions of the two energy storage mechanisms, and k_1v and $k_2v^{1/2}$ represent the contributions of pseudo-capacitance and diffusion control, respectively. As shown in Fig. 5c, the pseudo-capacitance contribution is evaluated from 0.2 to 1 mV s^{-1}, and the ratio increases from 81.8% to 91.7%. Fig. 5d shows that a high value of 91.7% can be achieved at 1 mV s^{-1}, indicating that excellent high-rate performance due to pseudo-capacitance contributions. As for Sb_2S_3 and Sb_2S_3 / C, the pseudo-capacitance contributions are shown in Figure S8, which are evaluated from 0.2 to 0.8 mV s^{-1}. The result indicates that both materials are diffusion type, with the ratio increases from 12.6 % to 22.6 % and 39.5 % to 64.7 %, respectively. To further understand the electron/ion transfer resistance of $AgSbS_2$ nanowires, the electrochemical impedance spectroscopy (EIS) of $AgSbS_2$ nanowires and Sb_2S_3 nanowires was measured in the frequency range of 600 kHz – 50 mHz, as shown in Figure S9. The Nyquist plot basically consists of the semicircle in high frequency and inclined line, corresponding to the charge-transfer resistance (Rct) and the Warburg impedance, respectively. After 100 cycles, the Rct of $AgSbS_2$ nanowires is lower than that of Sb_2S_3 nanowires, indicating that Ag-derived materials may improve the conductivity of anode materials. According to the constant current intermittent titration technique (GITT) to further analyze the lithiation kinetics process at the current density of 50 mA g^{-1} for 10 min, followed by 3 h relaxation. (Figure S10a). The diffusion coefficient of Li^+ can be studied according to Fick's second law:

$$D = \frac{4}{\pi\tau}\left(\frac{m_B V_M}{M_B S}\right)\left(\frac{\Delta E_S}{\Delta E_\tau}\right) \tag{3}$$

Where τ is the current pulse time, m_B, M_B and V_M are the mass, molar mass and molar volume of active material in the electrode, S is the surface area of the electrode, and ΔE_S and $\Delta E\tau$ are the deviation of each equilibrium voltage and voltage during the current pulse, respectively. The calculated D_{Li+} corresponds to different lithiation and de-lithiation states, as shown in Figures S10c and d. The D_{Li+} in the range of 10^{-12} to 10^{-10} cm^2 s^{-1} can be achieved

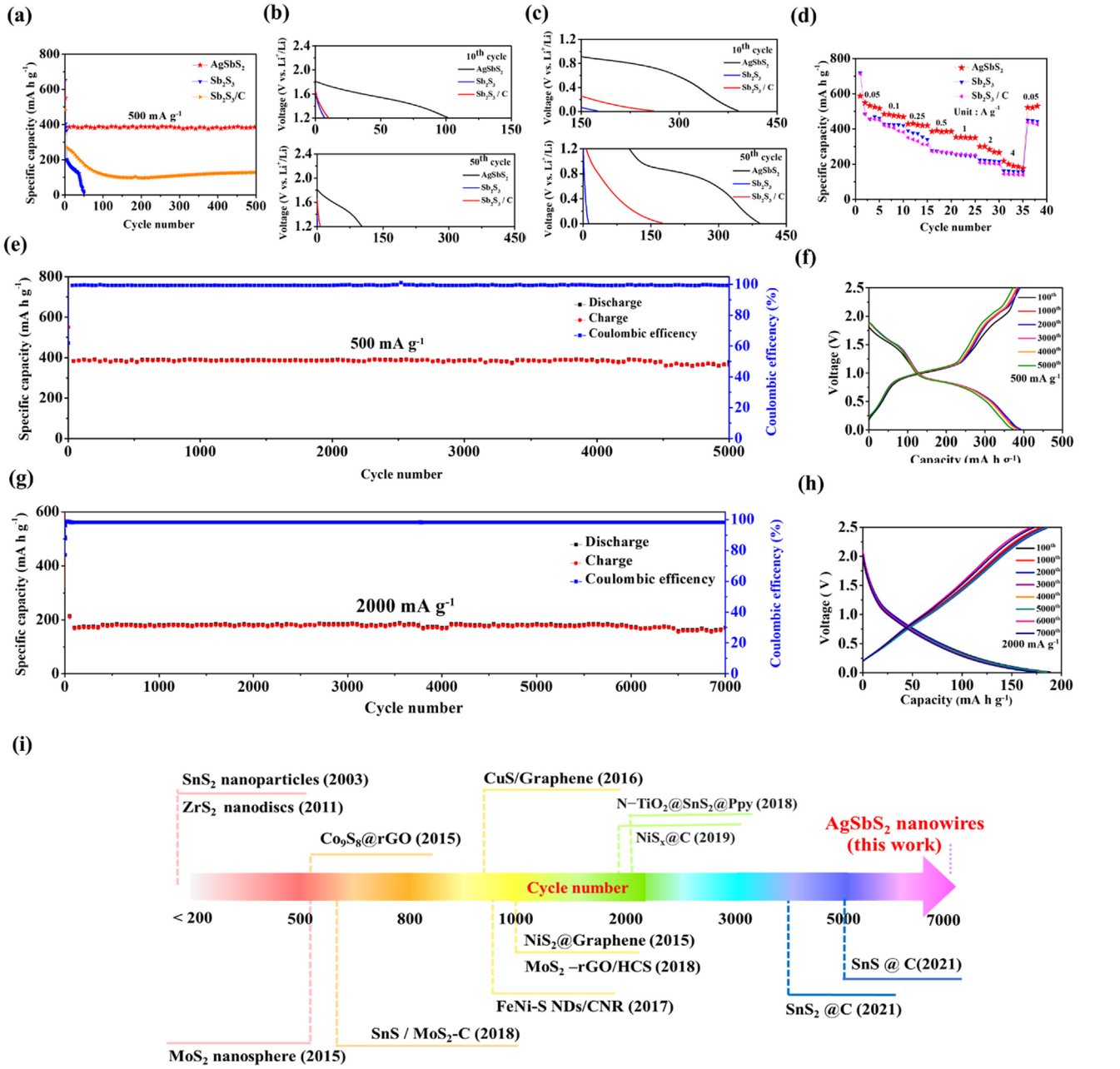

Fig. 4. Electrochemical properties of $AgSbS_2$, Sb_2S_3, and Sb_2S_3/C electrodes: (a) cycling performances at a current density of 500 mA g^{-1}, 10th and 50th discharge curves (b) from 2.4 to 1.2 V, and (c) from 1.2 to 0.01 V. (d) Rate performance of the $AgSbS_2$ electrode between 50 and 4000 mA g^{-1}. (e) Cycling performance and (f) galvanostatic charge/discharge curves of $AgSbS_2$ electrode at 500 mA g^{-1}. (g) Long-term cycle performance and (h) galvanostatic charge/discharge curves of the $AgSbS_2$ electrode at 2000 mA g^{-1}. (i) Comparison of cycling performance of $AgSbS_2$ and other S-based electrodes for LIBs.

for charge–discharge process. Figure S11 and Figure S12 also show the D_{Li}^{+} of Sb_2S_3 and Sb_2S_3 / C during the first charge–discharge process are in the range of $10^{-9} \sim 10^{-11}$, respectively. Moreover, to explore the electrochemical kinetics during charge–discharge process, *in-situ* EIS kinetic measurement of $AgSbS_2$ electrode was investigated. Fig. 5e shows the Nyquist plots of the $AgSbS_2$ electrode during initial discharge/charging process. In the initial cycle, as the $AgSbS_2$ electrode discharging from open circuit potential (OCP) to 1.5 V, the resistance increases slightly because the formation of the Li^+ insertion and SEI layer. After discharging from 1.5 V to 0.05 V, the resistance decreases significantly. When the electrode charging to 2.25 V, the resistance becomes significantly smaller, attributed that Ag can increase the conductivity and reduce the internal resistance. Fig. 5f shows the Nyquist plot of the *in-situ* EIS analysis of $AgSbS_2$ electrode in the 4th cycle to observe the electrochemical kinetics after the electrode is stabilized. When discharging to 0.5 V, the resistance decreases due to formation of a stable SEI layer. From discharging 0.5 to 0.05 V, there is no significant change in resistance, attributed to the stability of the Li^+ embedding process. When charging to 2 V, the resistance will return to the initial value, indicating that $AgSbS_2$ electrode exhibits a high reversibility after the first cycle. These results demonstrate the highly reversible kinetics of $AgSbS_2$ nanowires.

Fig. 6a shows the cyclic voltammetry curve (CV) of the $AgSbS_2$ electrode in the first six cycles between 0.01 and 2.5 V at a scan rate of 0.1 mV s^{-1}. During the first scan, the peak at 1.73 V may be due to Li^+ intercalate into $AgSbS_2$ without phase change. The

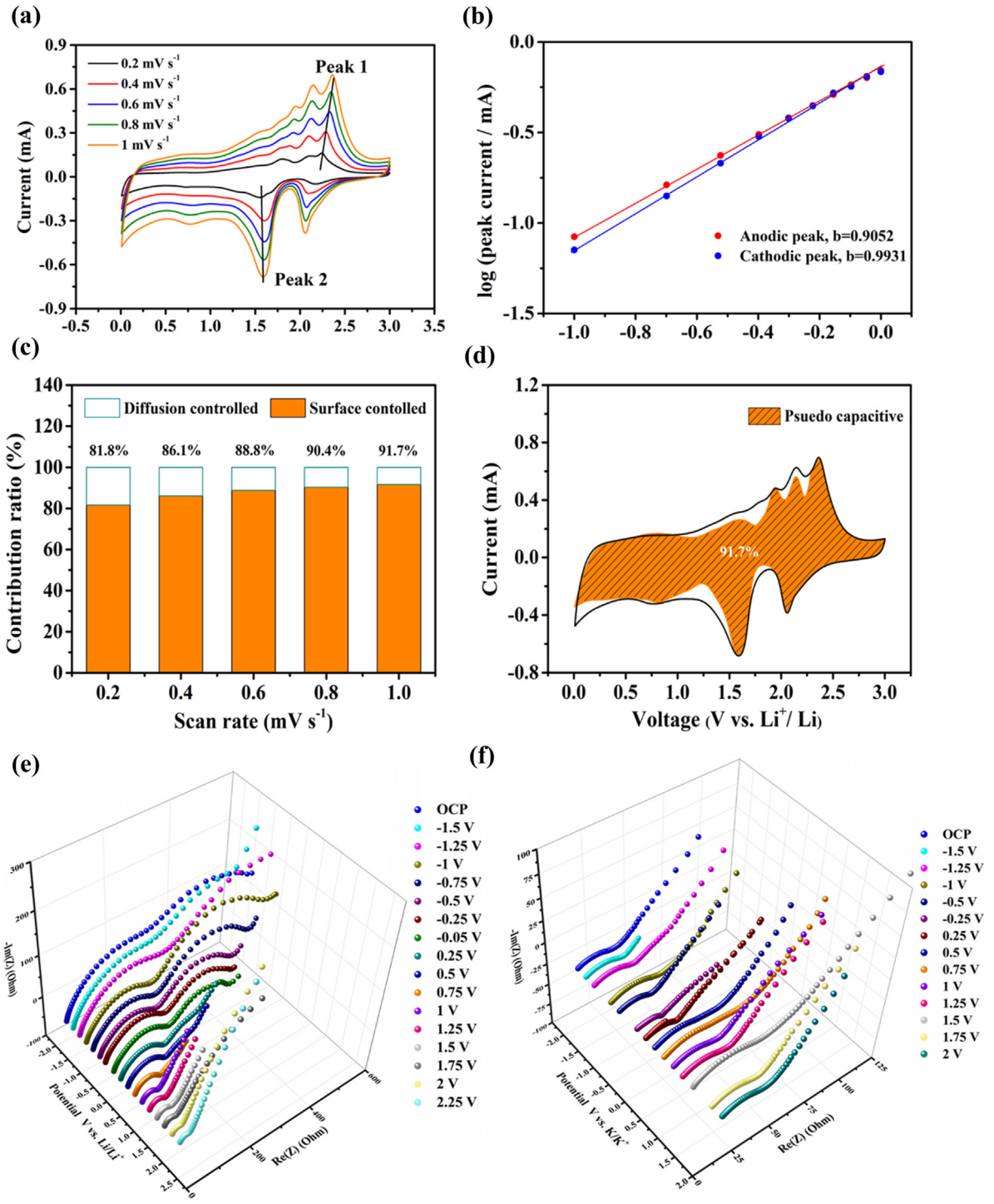

Fig. 5. (a) CV curves at various scan rates in the range of 0.2–1.0 mV s^{-1}, (b) linear fitting profiles of log(i, peak current) vs. log(v, scan rate), (c) the percentage of diffusion and capacitive-controlled capacity contributions at different scanning rates of $AgSbS_2$ and (d) the CV profiles displaying the Li-ions diffusion-controlled contribution at 1 mV s^{-1}. Nyquist plots of the $AgSbS_2$ electrode for (e) 1st and (f) 4th cycles.

reduction peak at 1.52 V corresponds to the conversion from $AgSbS_2$ to Sb, Ag and Li_2S. The reduction peak at 1.3 V may be attributed to the form of the solid electrolyte interface layer (SEI). A sharp reduction peak at about 0.8 V may be attributed to the alloying reaction of Sb to form Li_3Sb. The oxidation peaks at 0.35 V, 1.1 V and 2.1 V correspond to the dealloying reaction of Li_3-Sb and the conversion reaction of Li_2S to form Sb and S (amorphous), respectively. The almost overlapped CV curves of the following five cycles indicate excellent reversibility on $AgSbS_2$ anodes for LIBs. *Ex-situ* XRD was used to clarify the relationship between the intermediate phases and electrode potential, as shown in Fig. 6b, to understand the Li^+ storage mechanism of $AgSbS_2$ nanowires. At the initial state, the corresponding peak of $AgSbS_2$ can be clearly observed. When discharging from the OCP to 1.5 V, the peaks at 38.1° can be indexed to Ag (PDF 00–004-0783). When decreasing to 0.5 V, the peak at 26.6°, 27.1° and 38.1° can be ascribed to Li_2S, Li_3Sb (PDF 04–015-0235), and Ag, respectively. After complete lithiation to 0.01 V, the peaks at

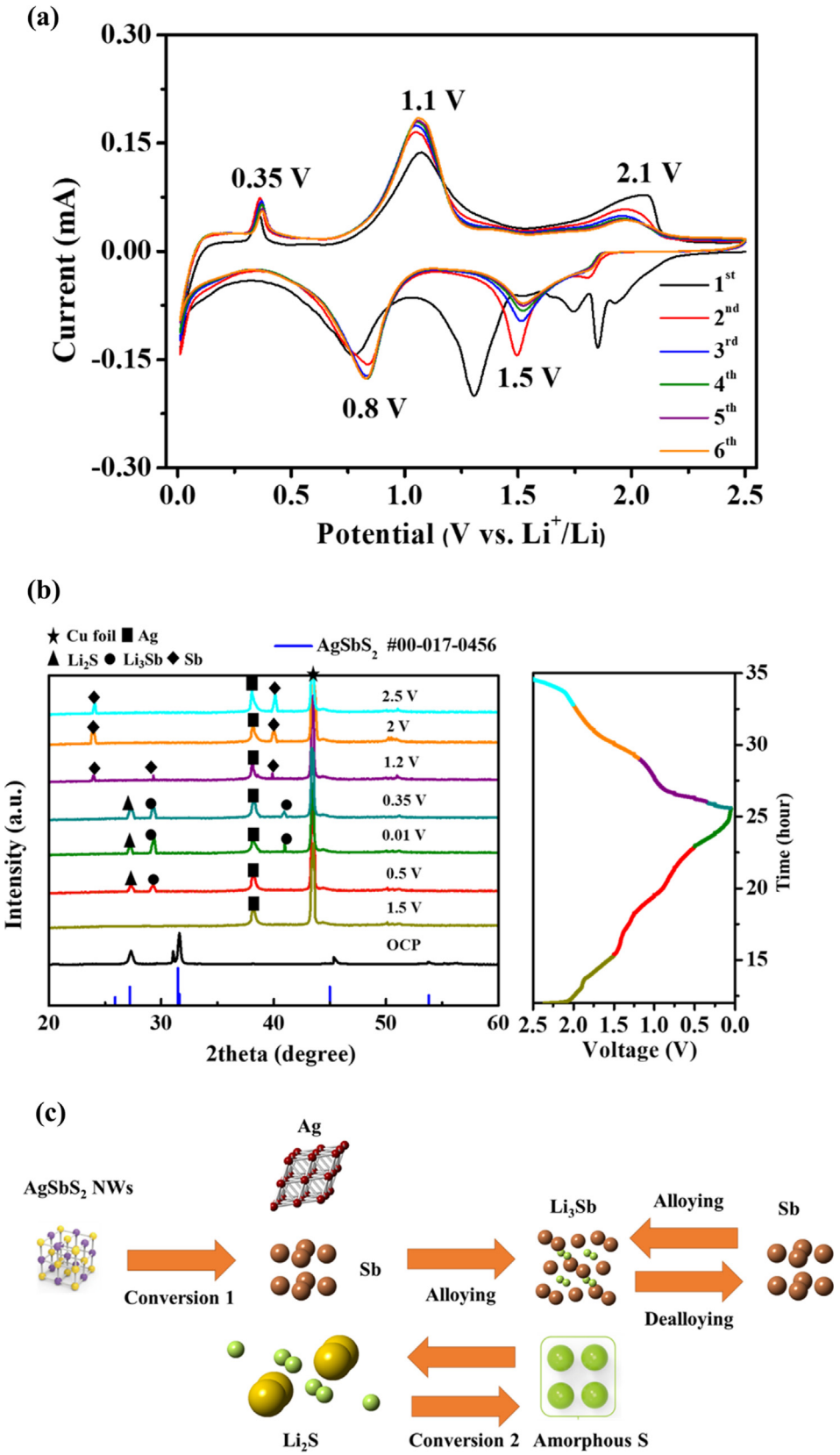

Fig. 6. (a) CV profiles of the initial six cycles at 0.1 mV s^{-1}. (b) *Ex-situ* XRD patterns of the $AgSbS_2$ electrode in the first cycle (left) and corresponding galvanostatic charge–discharge voltage profile (right). (c) Schematic view of the proposed electrochemical mechanism for $AgSbS_2$ during the charge/discharge process.

27.1° and 42.7° gradually increase. These two peaks are attributed to Li_3Sb, indicating that there is alloy reaction between Sb and Li^+. When charging to 1.2 V, two peaks appear at 24.8° and 41.7°, attributed to the reformation of Sb, accompanied by the disappearance of the Li_3Sb and Li_2S peaks. When charging to 2 and 2.5 V, Sb peak gradually increases, yet it can be found that there is no peak of $AgSbS_2$, indicating that the first cycle of discharging/charging process is an irreversible reaction. It is worth noting that the peak at 37° always exists during the lithiation-delithiation process. It can be inferred that Ag cannot react with Li^+, and can be used as a diluent to alleviate the volume expansion caused by intercalation/deintercalation of Li^+ and slow down the shuttle effect. Fig. 6b (right panel) shows the galvanostatic charge–discharge voltage profile in the first cycle corresponding to Fig. 6b (left panel). In addition, to further prove the *ex-situ* XRD results, Fig. 7-a-h show the *ex-situ* TEM, HRTEM and SAED images of the $AgSbS_2$ electrode at different discharge/charge states in the first cycle to further confirm the Li^+ storage mechanism. After discharging to 0.01 V, the TEM image of the $AgSbS_2$ electrode shows a nanowire morphology. The HRTEM image clearly shows that the lattice spacing of 0.234, 0.285, and 0.328 nm can be contributed to Ag (1 1 1), Li_2S (2 0 0) and Li_3Sb (2 0 0), respectively. It is worth noting that Ag will form boundary with Li_2S and Li_3Sb. The corresponding diffraction spots of the SAED test also confirmed the existence of Ag, Li_2S and Li_3Sb at this stage, which is consistent with the XRD results in Fig. 6b. After charging to 2.5 V, the structure of the nanowire remains unchanged. The HRTEM image shows the obvious lattice spacing of 0.263 and 0.234, which are assigned to the (1 1 1) plane of Sb and the (1 1 1) plane of Ag. Similarly, it can be found that Ag will form an interface with Sb. Ag forms boundary with the intermediates in the lithiation-delithiation process, indicating that Ag can have a synergistic effect with Sb and S, thereby improving the electrochemical performance of $AgSbS_2$. It is consistent with the SAED results. However, S element cannot be observed from both *ex-situ* XRD, HRTEM and SAED, yet the EDS images show S element after charging to 2.5 V in Fig. 7i-l. Therefore, it is speculated that amorphous S is formed after delithiation. These results indicate that this storage mechanism is an irreversible reaction. To better understand stability of $AgSbS_2$ nanowires, TEM images after 20 cycles were provided in Figure S13. Some nanoparticles are formed and the nanowires become thicker due to silver exsolution. Figure S14 and 15 show the *ex-situ* XPS spectrum of $AgSbS_2$ nanowires at 0.01 V and 3 V. When discharging to 0.01 V, the spectrum of Sb 3d and Li 1 s and the formation of polysulfide (Li_2S) can be observed. When charging to 3 V, it can be found the spectrum of Sb 3d, but the peak of polysulfide disappears. The results observed by *ex-situ* TEM are consistent with the results of *Ex-situ* XRD. According to above *ex situ* results, a reaction mechanism is inferred as shown by the schematic diagram in Fig. 6c. During the discharging process, $AgSbS_2$ undergoes conversion reaction producing Ag, Sb, and Li_2S. Then, Sb can react with Li to form Li_3Sb (alloying reaction). Accordingly, during the charging process, Li_3Sb and Li_2S are oxidized to Sb and S followed by dealloying reaction and conversion reaction, respectively. The process is summarized as follows:

First discharge.

$AgSbS_2 + 4e^- + 4Li^+ \rightarrow Ag + 2Li_2S + Sb$ (conversion reaction).

$Sb + 3Li^+ + 3e^- \rightarrow Li_3Sb$ (alloying reaction).

Discharge (reversible).

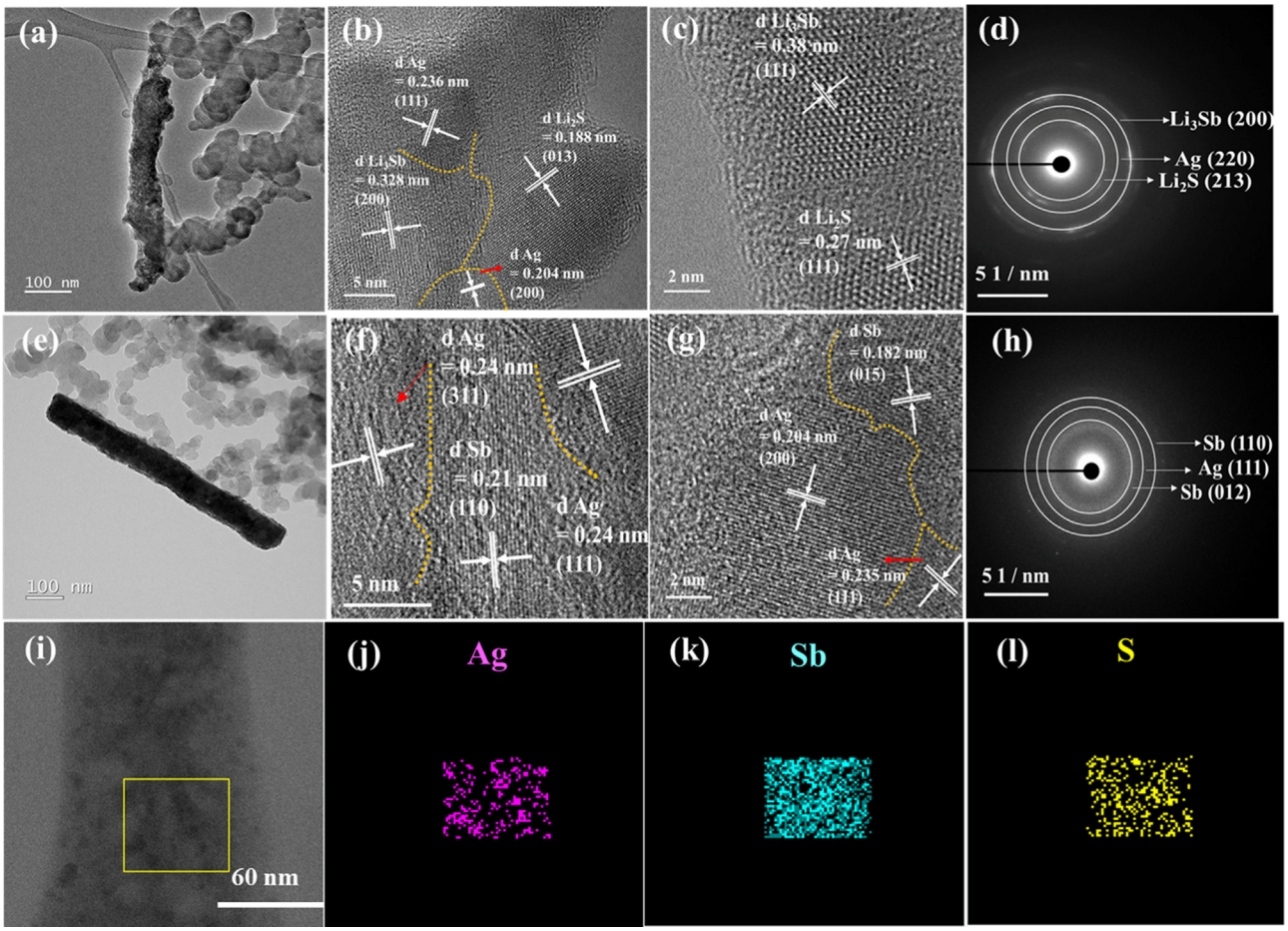

Fig. 7. (a) TEM, (b, c) HRTEM and (d) SAED images of the $AgSbS_2$ electrode at the initial fully discharged state. (e) TEM, (f, g) HRTEM and (h) SAED images of the $AgSbS_2$ electrode at the initial fully charged state. (i-l) EDS mapping images of Ag, S and Sb in $AgSbS_2$ nanowires at the initial fully charged state.

Li^+ + S (amorphous) → Li_2S (conversion reaction)
Sb + $3Li^+$ + $3e^-$ → Li_3Sb (alloying reaction).
Charging (reversible).
Li_3Sb → Sb + $3Li^+$ + $3e^-$ (dealloying reaction).
Li_2S → $2Li^+$ + S (amorphous) (conversion reaction).

Moreover, DFT calculations were carried out to investigate the role Ag to enhance the effect of metal sulfides on Li^+ storage. First, to explore whether the composition formed by Sb and S and Ag reduces the Li^+ adsorption energy of Sb or S. It can be observed that the adsorption energy of S-Li is −0.421 eV, and the adsorption energy of Ag/S-Li is reduced to −0.575 eV (Fig. 8a). The adsorption energy of Ag/Sb-Li (-1.055 eV) is lower than that of Sb-Li (-0.383 eV) (Fig. 8b). These results indicate that the formation of Ag can significantly enhance the adsorption of Sb or S on Li^+. Next, Fig. 8c shows the adsorption energy of Li on the Ag/Sb/S, Sb_2S_3, Ag, and Sb/S. The adsorption energies of Sb_2S_3-Li, Ag-Li and Sb/S-Li are −0.957 eV, −0.486 eV and −0.385 eV, respectively. It is worth noting that the adsorption energy of Ag/Sb/S-Li decreased to −1.022 eV, indicating that the addition of Ag has a great influence on the Li^+ adsorption energy of metal sulfides.

Although Ag does not react with Li^+ (the peak at 37° always exists during the lithiation-delithiation process), it stabilizes the structure of metal sulfides, performs excellent lithium ion storage and achieves rapid reaction kinetics, resulting in the following advantages for ultra-stable cycle life. First, it can be observed that in the CV curve of $AgSbS_2$ electrode the following 5 cycles almost overlap, except for the first cycle and the charge–discharge voltage plateaus are still very obvious after 1000 cycles, indicating its excellent reversibility. Second, it can be observed in *ex-situ* XRD and TEM of $AgSbS_2$ electrode shows the formation of Sb, Ag and Li_2S during the conversion process. It is worth noting that the HRTEM results show that Ag can form boundary with Li_3Sb and Li_2S during discharge, and also form boundary with Sb and S during charging, indicating that Ag will be closely mixed with other intermediate products after precipitation, which can stabilize the structure and prevent the shuttle effect of polysulfides. Therefore, the first circle is an irreversible reaction because Ag will no longer form $AgSbS_2$ with Sb and S during charging after the precipitation of Ag. It can be inferred that Ag will not react with lithium ions, and can be used as a diluent to alleviate the volume expansion caused by intercalation/deintercalation of Li^+. Third, as the simulation results, Ag/Sb/S is more beneficial to the adsorption of lithium ions than Sb_2S_3, because Ag enhances the ion kinetics of metal sulfides and the adsorption of Li^+, resulting in high specific capacity and excellent rate capability. Ag form boundary with the intermediate in the lithiation/delithiation process. It is speculated that Ag can have synergistic effect with Sb and S, thereby improving the cycle stability of the Sb-S based negative electrode. Compared with the literature data, it can be found that the cycle performance of metal sulfides is significantly improved through the addition of Ag than the addition of carbon materials. Fourth, through the relationship between the peak current and the scan rate in the different scan rates of CV curves, it can be observed that the capacitance contribution is as high as 91.7% at a scan rate of 1 mV s^{-1}, indicating that the excellent high-rate performance of $AgSbS_2$ because of the pseudo-capacitance, possibly because highly conductive Ag facilitates the migration of electrons and ions to maintain high conductivity. For example, Guo *et al.* reported that Ag/g-C_3N_4/Co_3O_4 composite delivers better initial discharge capacity and better cycling performance in lithium-oxygen batteries than that of the pure Co_3O_4 or Ag/g-C_3N_4 catalysts [69]. Finally, in the Nyquist diagram of the $AgSbS_2$ electrode during the initial discharge and charging, it is worth noting that the resistance is significantly reduced after the discharge to 1.5 V, which can be attributed to the precipitation of Ag to increase the electrode conductivity and reduce the internal resistance of the electrode. These theoretical analysis results are very consistent with the above-mentioned electrochemical and kinetic analysis results. Based on a large amount of data and discussion, the excellent lithium storage performance of $AgSbS_2$ electrode can be attributed to the synergistic effect of Ag. Therefore, the designed $AgSbS_2$ electrode material can provide excellent cycle stability and significant rate performance and stimulates the potential of $AgSbS_2$ used in energy storage devices.

In addition, to prove that Ag can effectively inhibit the shuttle effect, caused by the dissolution of sulfur in the electrolyte, the chemical adsorption experiments were performed by dispersing equal amounts of $AgSbS_2$ and Sb_2S_3 in the electrolyte (1 M $LiPF_6$

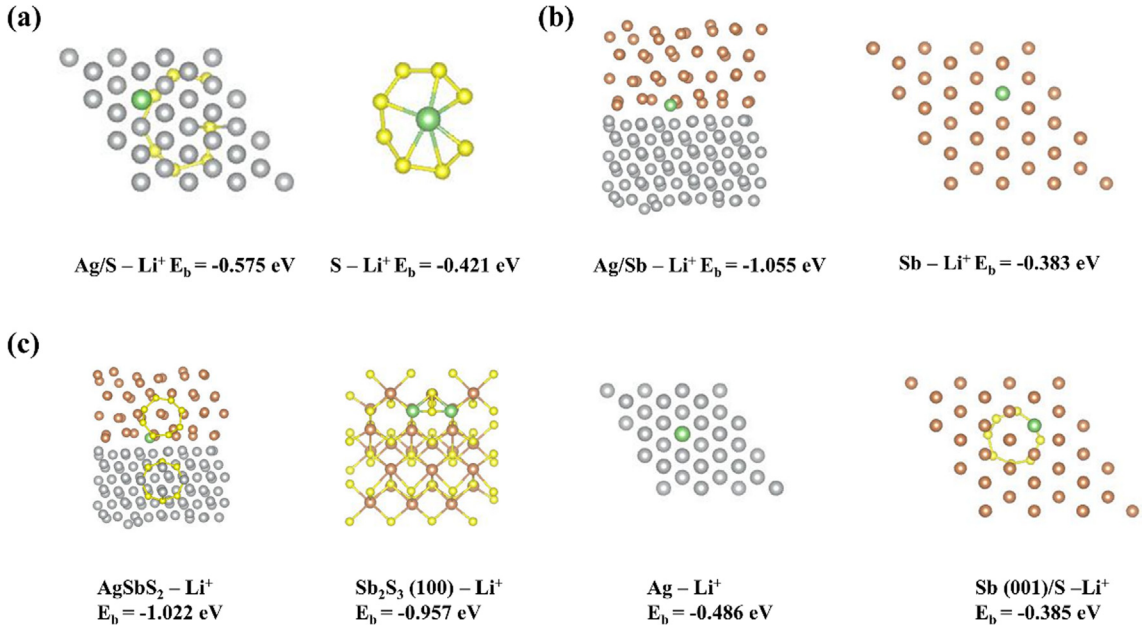

Fig. 8. Theoretical simulations and adsorption energy of (a) Ag/S and S, (b) Ag/Sb and Sb, and (c) $AgSbS_2$, Sb_2S_3, Ag and Sb models for Li^+. (Grey, red, yellow and green spheres denote Ag, Sb, S, and Li atoms, respectively). (For interpretation of the references to color in this figure legend, the reader is referred to the web version of this article.)

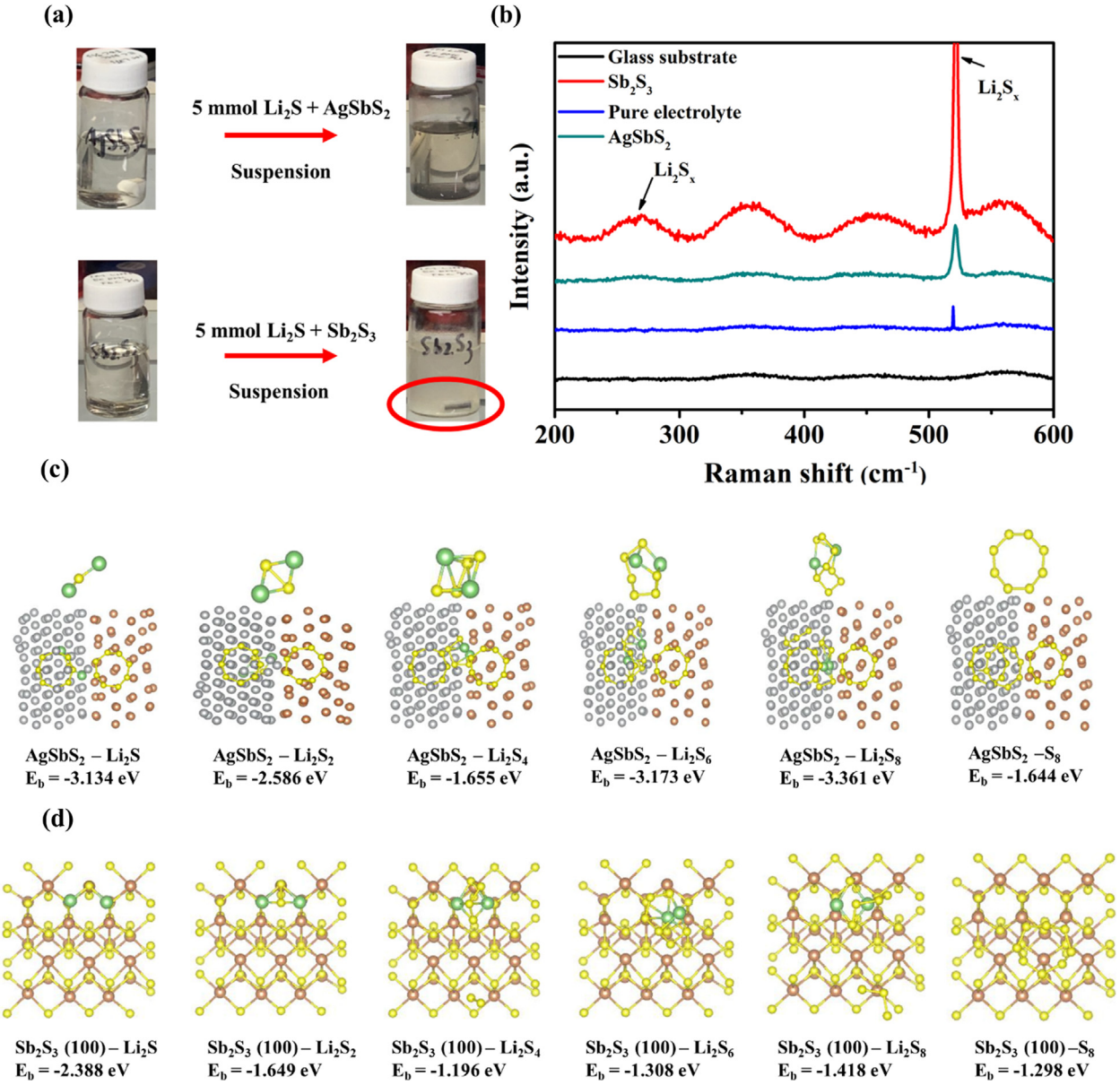

Fig. 9. (a) The chemical adsorption experiment of Li_2S on the $AgSbS_2$ and Sb_2S_3 electrodes. (b) Raman analyses of glass substrate, pure electrolyte, and the electrolytes with $AgSbS_2$ and Sb_2S_3 electrodes after testing. The side view and the adsorption energies of optimized geometries of Li_2S, Li_2S_2, Li_2S_4, Li_2S_6, Li_2S_8 and S_8 on (c) Ag/Sb/S and (d) Sb_2S_3 surfaces.

in EC: DMC: FEC) that contained 1 M Li_2S (Fig. 9a) [70]. After stirring for 3 h and standing for 24 h, the color change and precipitation of the solution were observed. Obviously, the electrolyte containing $AgSbS_2$ nanowires changed from the original yellow to almost colorless, confirming the strong adsorption of Li_2¬S by $AgSbS_2$ nanowires. The electrolyte containing Sb_2S_3 nanowire is slightly yellow and turbid, indicating that Sb_2S_3 cannot effectively adsorb polysulfide. Next, the Raman test was performed on the two electrolytes after the test and the pure electrolyte, and the results are shown in Fig. 9b. The glass substrate is used as the base. The Raman curve of the electrolyte containing $AgSbS_2$ is similar to that of pure electrolyte, but two excessive peaks at about ~ 268 and ~ 520.7 eV were clearly detected in the Raman spectra of the electrolyte containing Sb_2S_3, attributed to Li_2S_x [71]. Therefore, it can be inferred that Ag can effectively inhibit the shuttle effect. In addition, first-principles calculations based on DFT were carried out (Fig. 9c) in order to understand the strong adsorption effect of $AgSbS_2$ material on lithium polysulfides (LiPS). The Ag (1 1 1) and Sb (0 0 1) surfaces are selected based on HRTEM observations (Fig. 7), which should be the most exposed surfaces in the material. S is modeled by the amorphous phase. LiPS molecules were used for modeling on the surface of Ag/Sb/S and Sb_2S_3, respectively. Calculation the binding energy (Eb) between the LiPS material and Ag/Sb/S and Sb_2S_3 to evaluate the adsorption energy of LiPS. As a result, the calculated binding energies of Li_2S, Li_2S_2, Li_2S_4, Li2S6, Li_2S_8 and S_8 on Ag/Sb/S are −1.314, −2.586, −1.655, −3.173, −3.361 and −1.644 eV (lower than Sb2S3 of −2.388, −1.649, −1.196, −1.308, −1.418 and −1.298 eV), respectively, indicating that Ag/Sb/S is more conducive to the adsorption of LiPS. In other words, Ag can enhance the adsorption energy of metal sulfides on LiPSs. It can be observed that the sulfur atoms in LiPSs tend to bond with Ag atoms of Ag/Sb/S. The DFT results show that Ag

can indeed significantly enhance the interaction between LiPSs and Ag/Sb/S, which is beneficial to effectively inhibit the shuttle effect of polysulfides.

Based on the good cycle and rate performance of the half-cell, $AgSbS_2$ nanowires are used as an anode electrode combined with the layered positive electrode $Li(Ni_{0.5}Co_{0.3}Mn_{0.2})O_2$ to construct a lithium-ion full cell to prove the feasibility of being a LIB full battery anode. The lithium-ion full cell is tested in the voltage range of 0.5 V ~ 4.1 V, as shown in Fig. 10. Fig. 10a shows a schematic diagram of a $AgSbS_2//Li(Ni_{0.5}Co_{0.3}Mn_{0.2})O_2$ full cell configuration. Fig. 10b shows the discharge/charge curve of the full cell in the first three cycles at 500 mA g^{-1} and Figure S16 provides a detailed analysis of $LiNi_5Co_3Mn_2$. The specific capacity of 448.6 mA h g^{-1} is obtained in the first cycle. It is found that the discharge/charge curve has a clear platform due to the excellent electrochemical reaction kinetics of the cathode and anode. Moreover, the full cell

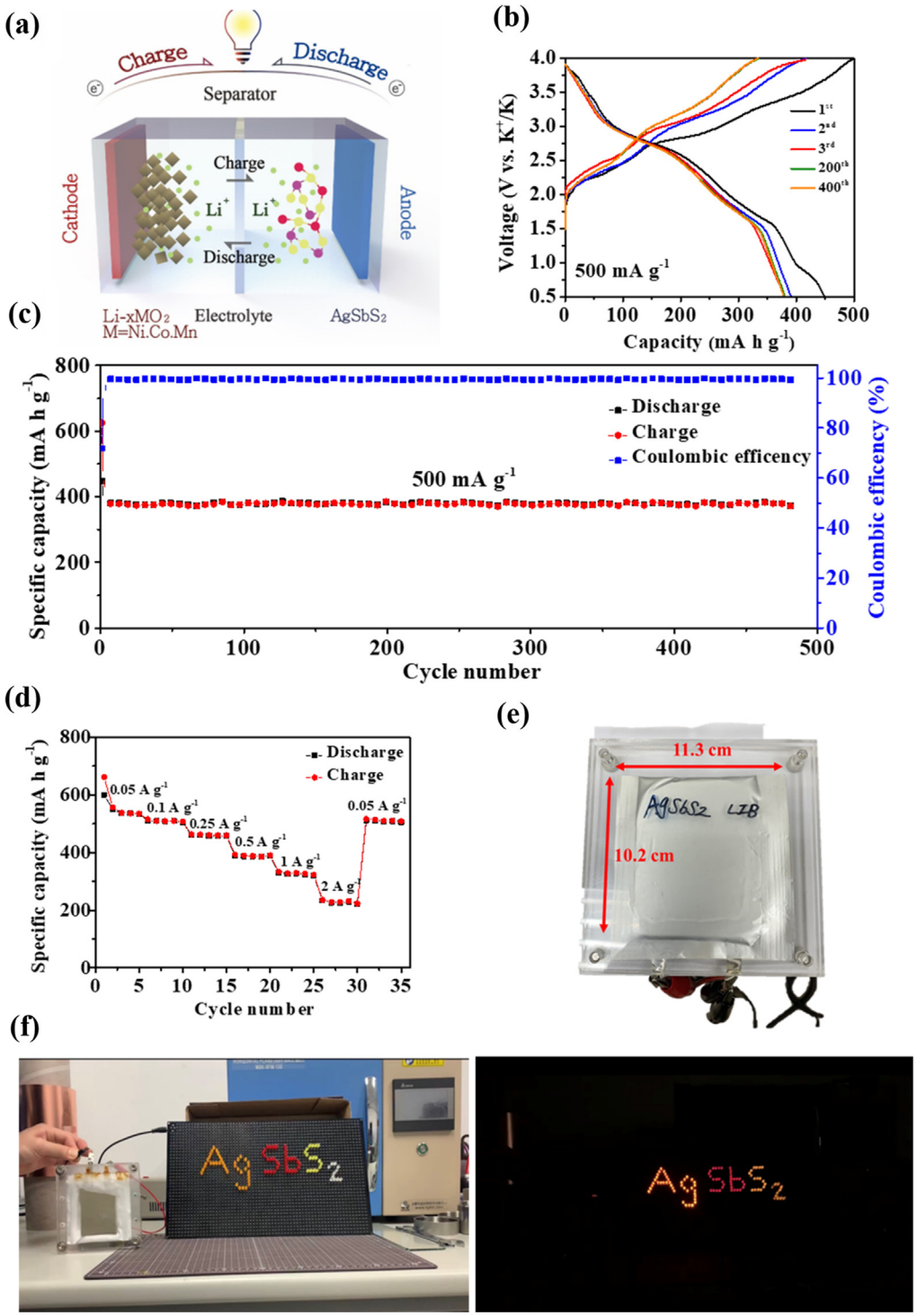

Fig. 10. (a) LIB full cell using a $AgSbS_2$ anode and a $LiNi_5Co_3Mn_2$ cathode. (b) Galvanostatic charge/discharge curves of the initial three cycles at 500 mA g^{-1}. (c) Cycling performances at 500 mA g^{-1} and (d) rate performances between 50 and 2000 mA g^{-1}. (e) The optical image of pouch-type full cell with a length of 11.3 cm and width of 10.2 cm. (f) The photograph of the $AgSbS_2//$ $LiNi_5Co_3Mn_2$ pouch-type cells lighting up the LED.

shows excellent long-term cycle performance and Coulombic efficiency. The reversible capacity can be maintained at close to 400 mA h g^{-1} for nearly 500.

cycles at 500 mA g^{-1} with Coulombic efficiency of 99.5% (Fig. 10c). When the current density is 0.05, 0.1, 0.25, 0.5, 1, and 2 A g^{-1}, the specific capacity is 534.6, 505.1, 456.7, 388.5, 320, and 221.3 mA h g^{-1}, respectively. When the current density is returned to 0.05 A g^{-1}, a specific capacity of 530.9 mA h g^{-1} can be achieved (Fig. 10d). In addition, a pouch-type $AgSbS_2$// $Li(Ni_{0.5}Co_{0.3}Mn_{0.2})O_2$ battery can power a light-emitting diode (LED) screen composed of 16 yellow bulbs, 33 red bulbs and 40 orange bulbs, demonstrating its potential application prospects for electronic products, as shown in Fig. 10e and f. The above full battery results indicate that the $AgSbS_2$ anodes with good cycling stability and faster reaction rate have good potential in the further development of LIBs.

4. Conclusion

We report a new type of silver-based metal sulfide nanostructures to achieve super stable cycle life of LIBs. After the silver is precipitated out, it forms tiny nano-crystals that can interact with Sb and Sb to form a tightly connected complex and not affect the morphology of the nanowires. The presence of silver in the electrode plays a multiple and key positive impact on the improvement of electrochemical effects. Silver, thanks to its nature high conductivity, can greatly decrease the resistance of the battery when the battery is in operation, making the battery perform well during high-rate charging and discharging. Moreover, due to the presence of Ag, the adsorption of Li^+ is better than that of Sb and S, which helps to reduce the polarization of Li^+ or adsorption and diffusion and achieve capacitive storage phenomena. The $AbSbS_2$ become a super stable battery electrode, reaching a Coulombic efficiency of approximately 99% per cycle and a capacity retention of 90.6% in the 100th cycle at 7000 cycles at 2 A g^{-1}. This extraordinary cycle life far exceeds the result reported to date. More importantly, silver can also effectively capture sulfur, making the shutting effect that often occurs in sulfide-based electrodes effective Inhibition. Using $AbSbS_2$ nanowires as stable anodes for LIBs does not require complex, high-temperature and multi-step procedures, we believe this study scientifically clarifies that the $AbSbS_2$ electrode provides a new perspective for the development of metal sulfides anodes for LIBs.

The authors declare that they have no known competing financial interests or personal relationships that could have appeared to influence the work reported in this paper.

CRediT authorship contribution statement

Sheng-Feng Ho: Conceptualization, Methodology, Data curation. **Yi-Chun Yang:** Methodology, Data curation. **Hsing-Yu Tuan:** Conceptualization, Resources, Supervision, Writing – review & editing.

Declaration of Competing Interest

The authors declare that they have no known competing financial interests or personal relationships that could have appeared to influence the work reported in this paper.

Acknowledgements

This work was supported by the financial support from the 2030 Cross-Generation Young Scholars Program by Ministry of Science and Technology, Taiwan (MOST 111-2628-E-007-008).

Appendix A. Supplementary data

Supplementary data to this article can be found online at https://doi.org/10.1016/j.jcis.2022.04.020.

References

[1] K.J. Griffith, K.M. Wiaderek, G. Cibin, L.E. Marbella, C.P. Grey, Niobium tungsten oxides for high-rate lithium-ion energy storage, Nat. 559 (7715) (2018) 556–563.
[2] X. Lv, W. Wei, B. Huang, Y. Dai, Achieving high energy density for lithium-ion battery anodes by Si/C nanostructure design, J. Mater. Chem. A 7 (5) (2019) 2165–2171.
[3] M.-S. Balogun, H. Yang, Y. Luo, W. Qiu, Y. Huang, Z.-Q. Liu, Y. Tong, Achieving high gravimetric energy density for flexible lithium-ion batteries facilitated by core–double-shell electrodes, Energy Environ Sci 11 (7) (2018) 1859–1869.
[4] B. Ji, F. Zhang, M. Sheng, X. Tong, Y. Tang, A Novel and Generalized Lithium-Ion-Battery Configuration utilizing Al Foil as Both Anode and Current Collector for Enhanced Energy Density, Adv. Mater. 29 (7) (2017) 1604219.
[5] C.-Y. Huang, C.-W. Huang, M.-C. Wu, J. Patra, T.X. Nguyen, M.-T. Chang, O. Clemens, J.-M. Ting, J. Li, J.-K. Chang, Atomic-scale investigation of Lithiation/Delithiation mechanism in High-entropy spinel oxide with superior electrochemical performance, Chem. Eng. J. 420 (2021).
[6] S. Gu, Z. Bai, S. Majumder, B. Huang, G. Chen, Conductive metal–organic framework with redox metal center as cathode for high rate performance lithium ion battery, J. Power Sources 429 (2019) 22–29.
[7] S. Chen, Z. Chen, X. Xu, C. Cao, M. Xia, Y. Luo, Scalable 2D Mesoporous Silicon Nanosheets for High-Performance Lithium-Ion Battery Anode, Small 14 (12) (2018) 1703361.
[8] Y. Xia, T. Zhao, X. Zhu, Y. Zhao, H. He, C.-T. Hung, X. Zhang, Y. Chen, X. Tang, J. Wang, Inorganic-organic competitive coating strategy derived uniform hollow gradient-structured ferroferric oxide-carbon nanospheres for ultra-fast and long-term lithium-ion battery, Nat. Commun 12 (1) (2021) 1–10.
[9] J. Choi, W.-S. Kim, K.-H. Kim, S.-H. Hong, Sn4P3–C nanospheres as high capacitive and ultra-stable anodes for sodium ion and lithium ion batteries, J. Mater. Chem. A 6 (36) (2018) 17437–17443.
[10] Q. Yang, J. Huang, Y. Li, Y. Wang, J. Qiu, J. Zhang, H. Yu, X. Yu, H. Li, L. Chen, Surface-protected LiCoO2 with ultrathin solid oxide electrolyte film for high-voltage lithium ion batteries and lithium polymer batteries, J. Power Sources 388 (2018) 65–70.
[11] L. Zhang, J. Deng, L. Liu, W. Si, S. Oswald, L. Xi, M. Kundu, G. Ma, T. Gemming, S. Baunack, Hierarchically designed SiOx/SiOy bilayer nanomembranes as stable anodes for lithium ion batteries, Adv. Mater. 26 (26) (2014) 4527–4532.
[12] H. Zhao, Y. Wei, C. Wang, R. Qiao, W. Yang, P.B. Messersmith, G. Liu, Mussel-inspired conductive polymer binder for Si-alloy anode in lithium-ion batteries, ACS Appl. Mater. Interfaces 10 (6) (2018) 5440–5446.
[13] Q. Li, H. Li, Q. Xia, Z. Hu, Y. Zhu, S. Yan, C. Ge, Q. Zhang, X. Wang, X. Shang, Extra storage capacity in transition metal oxide lithium-ion batteries revealed by in situ magnetometry, Nat. Mater. 20 (1) (2021) 76–83.
[14] W. Weng, J. Lin, Y. Du, X. Ge, X. Zhou, J. Bao, Template-free synthesis of metal oxide hollow micro-/nanospheres via Ostwald ripening for lithium-ion batteries, J. Mater. Chem. A 6 (22) (2018) 10168–10175.
[15] W. Cheng, H. Di, Z. Shi, D. Zhang, Synthesis of ZnS/CoS/CoS2@N-doped carbon nanoparticles derived from metal-organic frameworks via spray pyrolysis as anode for lithium-ion battery, J. Alloys Compd. 831 (2020).
[16] D. Chen, H. Quan, G.-S. Wang, L. Guo, Hollow [alpha]-MnS Spheres and Their Hybrids with Reduced Graphene Oxide: Synthesis, Microwave Absorption, and Lithium Storage Properties, ChemPlusChem 78 (8) (2013) 843.
[17] A.C. Mendhe, S. Majumder, N. Nair, B.R. Sankapal, Core-shell cadmium sulphide@silver sulphide nanowires surface architecture: Design towards photoelectrochemical solar cells, J. Colloid Interface Sci. 587 (2021) 715–726.
[18] S.S. Karade, B.R. Sankapal, Room temperature PEDOT: PSS encapsulated MWCNTs thin film for electrochemical supercapacitor, J. Electroanal. Chem. 771 (2016) 80–86.
[19] N. Sonawane, K. Gurav, R. Ahire, J. Kim, B. Sankapal, CdS nanowires with PbS nanoparticles surface coating as room temperature liquefied petroleum gas sensor, Sensors and Actuators A: Physical 216 (2014) 78–83.
[20] J. Xie, J. Xia, Y. Yuan, L. Liu, Y. Zhang, S. Nie, H. Yan, X. Wang, Sb2S3 embedded in carbon–silicon oxide nanofibers as high-performance anode materials for lithium-ion and sodium-ion batteries, J. Power Sources 435 (2019).
[21] K. Zhang, F. Chen, H. Pan, L. Wang, D. Wang, Y. Jiang, L. Wang, Y. Qian, Study on the effect of transition metal sulfide in lithium–sulfur battery, Inorg. Chem. Front. 6 (2) (2019) 477–481.
[22] Q. Pan, Z. Tong, Y. Su, S. Qin, Y. Tang, Energy Storage Mechanism, Challenge and Design Strategies of Metal Sulfides for Rechargeable Sodium/Potassium-Ion Batteries, Adv. Funct. Mater. 31 (37) (2021) 2103912.
[23] L. Yue, D. Wu, Z. Wu, W. Zhao, D. Wang, B. Zhong, Q. Liu, Y. Liu, S. Gao, A.M. Asiri, A MnS/FeS2 heterostructure with a high degree of lattice matching anchored into carbon skeleton for ultra-stable sodium-ion storage, J. Mater. Chem. A 9 (42) (2021) 24024–24035.
[24] W. Zhao, L. Gao, L. Yue, X. Wang, Q. Liu, Y. Luo, T. Li, X. Shi, A.M. Asiri, X. Sun, Constructing a hollow microflower-like ZnS/CuS@C heterojunction as an effective ion-transport booster for an ultrastable and high-rate sodium storage anode, J. Mater. Chem. A 9 (10) (2021) 6402–6412.

[25] W. Zhao, X. Wang, X. Ma, L. Yue, Y. Ren, T. Li, J. Xia, L. Zhang, Q. Liu, Y. Luo, Functional integration of hierarchical core–shell architectures via vertically arrayed ultrathin CuSe nanosheets decorated on hollow CuS microcages targeting highly effective sodium-ion storage, J. Mater. Chem. A 9 (48) (2021) 27615–27628.
[26] J. Chu, W.A. Wang, J. Feng, C.-Y. Lao, K. Xi, L. Xing, K. Han, Q. Li, L. Song, P. Li, Deeply nesting zinc sulfide dendrites in tertiary hierarchical structure for potassium ion batteries: enhanced conductivity from interior to exterior, ACS Nano 13 (6) (2019) 6906–6916.
[27] J. He, Y. Chen, A. Manthiram, Metal sulfide-decorated carbon sponge as a highly efficient electrocatalyst and absorbant for polysulfide in high-loading Li2S batteries, Adv. Energy Mater. 9 (20) (2019) 1900584.
[28] S.-C. Lim, M.-C. Hsiao, M.-D. Lu, Y.-L. Tung, H.-Y. Tuan, Synthesis of germanium–platinum nanoparticles as high-performance catalysts for spray-deposited large-area dye-sensitized solar cells (DSSC) and the hydrogen evolution reaction (HER), Nanoscale 10 (35) (2018) 16657–16666.
[29] S.-C. Lu, M.-C. Hsiao, M. Yorulmaz, L.-Y. Wang, P.-Y. Yang, S. Link, W.-S. Chang, H.-Y. Tuan, Single-crystalline copper nano-octahedra, Chem. Mater. 27 (24) (2015) 8185–8188.
[30] S. Foley, H. Geaney, G. Bree, S. Mukherjee, M.J. Zaworotko, K.M. Ryan, Layered Bimetallic Metal-Organic Material Derived Cu2SnS3/SnS2/C Composite for Anode Applications in Lithium-Ion Batteries, ChemElectroChem (23) (2018) 3764–3770.
[31] H.-J. Yang, C.-Y. Chen, F.-W. Yuan, H.-Y. Tuan, Designed synthesis of solid and hollow Cu2–xTe nanocrystals with tunable near-infrared localized surface plasmon resonance, J. Phys. Chem. C 117 (42) (2013) 21955–21964.
[32] X. Ni, T. Qian, X. Liu, N. Xu, J. Liu, C. Yan, High Lithium Ion Conductivity LiF/GO Solid Electrolyte Interphase Inhibiting the Shuttle of Lithium Polysulfides in Long-Life Li–S Batteries, Adv. Funct. Mater. 28 (13) (2018) 1706513.
[33] D. Liu, C. Zhang, G. Zhou, W. Lv, G. Ling, L. Zhi, Q.H. Yang, Catalytic effects in lithium–sulfur batteries: promoted sulfur transformation and reduced shuttle effect, Adv. Sci. 5 (1) (2018) 1700270.
[34] W.G. Lim, C. Jo, A. Cho, J. Hwang, S. Kim, J.W. Han, J. Lee, Approaching ultrastable high-rate Li–S batteries through hierarchically porous titanium nitride synthesized by multiscale phase separation, Adv. Mater. 31 (3) (2019) 1806547.
[35] H.-Y. Tuan, A. Ghezelbash, B.A. Korgel, Silicon nanowires and silica nanotubes seeded by copper nanoparticles in an organic solvent, Chem. Mater. 20 (6) (2008) 2306–2313.
[36] S.-H. Chang, B.-C. Chiu, T.-L. Gao, S.-L. Jheng, H.-Y. Tuan, Selective synthesis of copper gallium sulfide (CuGaS2) nanostructures of different sizes, crystal phases, and morphologies, CrystEngComm 16 (16) (2014) 3323–3330.
[37] F.-W. Yuan, H.-J. Yang, H.-Y. Tuan, Seeded silicon nanowire growth catalyzed by commercially available bulk metals: broad selection of metal catalysts, superior field emission performance, and versatile nanowire/metal architectures, J. Mater. Chem. A 21 (36) (2011) 13793–13800.
[38] S. Imtiaz, Z. Ali Zafar, R. Razaq, D. Sun, Y. Xin, Q. Li, Z. Zhang, L. Zheng, Y. Huang, J.A. Anderson, Electrocatalysis on separator modified by molybdenum trioxide nanobelts for lithium–sulfur batteries, Adv. Mater. Interfaces 5 (15) (2018) 1800243.
[39] S. Gao, N. Wang, S. Li, D. Li, Z. Cui, G. Yue, J. Liu, X. Zhao, L. Jiang, Y. Zhao, A Multi-Wall Sn/SnO2@ Carbon Hollow Nanofiber Anode Material for High-Rate and Long-Life Lithium-Ion Batteries, Angew. Chem. Int. Ed. 59 (6) (2020) 2465–2472.
[40] Q. Ma, H. Song, Q. Zhuang, J. Liu, Z. Zhang, C. Mao, H. Peng, G. Li, K. Chen, Iron-nitrogen-carbon species boosting fast conversion kinetics of Fe1-xS@C nanorods as high rate anodes for lithium ion batteries, Chem. Eng. J. 338 (2018) 726–733.
[41] S. Du, C. Wu, L. Ao, X. Zhou, K. Jiang, L. Shang, Y. Li, J. Zhang, Z. Hu, J. Chu, Significantly enhanced lithium storage by in situ grown CoS2@ MoS2 core–shell nanorods anchored on carbon cloth, Chem. Eng. J. 420 (2021).
[42] H. Wang, Z. Tong, R. Yang, Z. Huang, D. Shen, T. Jiao, X. Cui, W. Zhang, Y. Jiang, C.S. Lee, Electrochemically Stable Sodium Metal-Tellurium/Carbon Nanorods Batteries, Adv. Energy Mater. 9 (48) (2019) 1903046.
[43] P. Bhattacharya, J.H. Lee, K.K. Kar, H.S. Park, Carambola-shaped SnO2 wrapped in carbon nanotube network for high volumetric capacity and improved rate and cycle stability of lithium ion battery, Chem. Eng. J. 369 (2019) 422–431.
[44] Z. Wang, K. Dong, D. Wang, F. Chen, S. Luo, Y. Liu, C. He, C. Shi, N. Zhao, Monodisperse multicore-shell SnSb@SnOx/SbOx@C nanoparticles space-confined in 3D porous carbon networks as high-performance anode for Li-ion and Na-ion batteries, Chem. Eng. J. 371 (2019) 356–365.
[45] S.-J. Lu, Z.-T. Wang, X.-H. Zhang, Z.-J. He, H. Tong, Y.-J. Li, J.-C. Zheng, In situ-formed hollow cobalt sulfide wrapped by reduced graphene oxide as an anode for high-performance lithium-ion batteries, ACS Appl. Mater. Interfaces 12 (2) (2020) 2671–2678.
[46] Y. Zhang, P. Wang, Y. Yin, X. Zhang, L. Fan, N. Zhang, K. Sun, Heterostructured SnS-ZnS@C hollow nanoboxes embedded in graphene for high performance lithium and sodium ion batteries, Chem. Eng. J. 356 (2019) 1042–1051.
[47] H. Zhang, A. Hao, Z. Sun, X. Ning, J. Guo, Y. Lv, D. Jia, Boosting the performance of half/full lithium-ion batteries by designing smart architecture anode of SnS2 nanosheet coating on NiCo2S4 hollow spheres, J. Alloys Compd. 847 (2020).
[48] Z. Jiang, Z. Zeng, W. Hu, Z. Han, S. Cheng, J. Xie, Diluted high concentration electrolyte with dual effects for practical lithium-sulfur batteries, Energy Storage Mater. 36 (2021) 333–340.
[49] Z. Zhang, Y. Fu, C. Zhou, Y. Lai, Facile synthesis of CuSbS2 blocks, and their lithium ion storage performance, J. Electron. Mater. 44 (1) (2015) 252–257.
[50] P. Yadav, N. Sharma, A. Patrike, Y.M. Sabri, L.A. Jones, M.V. Shelke, Electrochemical Evaluation of the Stability and Capacity of r-GO-Wrapped Copper Antimony Chalcogenide Anode for Li-Ion battery, ChemElectroChem 7 (15) (2020) 3291–3300.
[51] G. Kresse, D. Joubert, From ultrasoft pseudopotentials to the projector augmented-wave method, Phys. Rev. B 59 (3) (1999) 1758.
[52] G. Kresse, J. Furthmüller, Efficient iterative schemes for ab initio total-energy calculations using a plane-wave basis set, Phys. Rev. B 54 (16) (1996) 11169.
[53] S. Das, M. Bououdina, C. Manoharan, The influence of cationic surfactant CTAB on optical, dielectric and magnetic properties of cobalt ferrite nanoparticles, Ceram. Int. 46 (8) (2020) 11705–11716.
[54] Y. Zhang, J. Tian, K. Jiang, J. Huang, F. Li, P. Wang, H. Fan, Y. Song, AgSbS2 thin film fabricated by in-situ gas-solid reaction and employed in solar cells as a light absorber, Mater. Lett. 232 (2018) 82–85.
[55] H. Hu, M. Mo, B. Yang, X. Zhang, Q. Li, W. Yu, Y. Qian, Solvothermal synthesis of Sb2S3 nanowires on a large scale, J. Cryst. Growth 258 (1–2) (2003) 106–112.
[56] H. Mukaibo, A. Yoshizawa, T. Momma, T. Osaka, Particle size and performance of SnS2 anodes for rechargeable lithium batteries, J. Power Sources 119 (2003) 60–63.
[57] N. Mahmood, C. Zhang, J. Jiang, F. Liu, Y. Hou, Multifunctional Co3S4/graphene composites for lithium ion batteries and oxygen reduction reaction, Chemistry–A, European Journal 19 (16) (2013) 5183–5190.
[58] D.H. Youn, C. Jo, J.Y. Kim, J. Lee, J.S. Lee, Ultrafast synthesis of MoS2 or WS2-reduced graphene oxide composites via hybrid microwave annealing for anode materials of lithium ion batteries, J. Power Sources 295 (2015) 228–234.
[59] R. Jin, Y. Jiang, G. Li, Y. Meng, Amorphous carbon coated multiwalled carbon nanotubes@ transition metal sulfides composites as high performance anode materials for lithium ion batteries, Electrochim. Acta 257 (2017) 20–30.
[60] H. Wang, S. Lu, Y. Chen, L. Han, J. Zhou, X. Wu, W. Qin, Graphene/Co9S8 nanocomposite paper as a binder-free and free-standing anode for lithium-ion batteries, J. Mater. Chem. A 3 (47) (2015) 23677–23683.
[61] H. Li, Y. Wang, J. Huang, Y. Zhang, J. Zhao, Microwave-assisted synthesis of CuS/graphene composite for enhanced lithium storage properties, Electrochim. Acta 225 (2017) 443–451.
[62] Q. Chen, W. Chen, J. Ye, Z. Wang, J.Y. Lee, L-Cysteine-assisted hydrothermal synthesis of nickel disulfide/graphene composite with enhanced electrochemical performance for reversible lithium storage, J. Power Sources 294 (2015) 51–58.
[63] X. Hu, Y. Li, G. Zeng, J. Jia, H. Zhan, Z. Wen, Three-dimensional network architecture with hybrid nanocarbon composites supporting few-layer MoS2 for lithium and sodium storage, ACS Nano 12 (2) (2018) 1592–1602.
[64] X. Gao, J. Wang, D. Zhang, K. Adair, K. Feng, N. Sun, H. Zheng, H. Shao, J. Zhong, Y. Ma, Carbon coated bimetallic sulfide nanodots/carbon nanorod heterostructure enabling long-life lithium-ion batteries, J. Mater. Chem. A 5 (48) (2017) 25625–25631.
[65] Q. Pan, F. Zheng, Y. Wu, X. Ou, C. Yang, X. Xiong, M. Liu, MoS2-covered SnS nanosheets as anode material for lithium-ion batteries with high capacity and long cycle life, J. Mater. Chem. A 6 (2) (2018) 592–598.
[66] L. Wu, J. Zheng, L. Wang, X. Xiong, Y. Shao, G. Wang, J.H. Wang, S. Zhong, M. Wu, PPy-encapsulated SnS2 nanosheets stabilized by defects on a TiO2 support as a durable anode material for lithium-ion batteries, Angewandte Chemie 131 (3) (2019) 821–825.
[67] Q. Li, L. Li, P. Wu, N. Xu, L. Wang, M. Li, A. Dai, K. Amine, L. Mai, J. Lu, Silica restricting the sulfur volatilization of nickel sulfide for high-performance lithium-ion batteries, Adv. Energy Mater. 9 (43) (2019) 1901153.
[68] Q. Cheng, X. Yu, Structural engineering of metal–organic framework derived tin sulfides for advanced Li/Na storage, J. Mater. Chem. A 9 (18) (2021) 11381–11396.
[69] Q. Guo, C. Zhang, C. Zhang, S. Xin, P. Zhang, Q. Shi, D. Zhang, Y. You, Co3O4 modified Ag/g-C3N4 composite as a bifunctional cathode for lithium-oxygen battery, J. Energy Chem. 41 (2020) 185–193.
[70] K. Zhang, W. Cai, Y. Liu, G. Hu, W. Hu, Y. Kong, X. Zhang, L. Wang, G. Li, Nitrogen-doped carbon embedded with Ag nanoparticles for bidirectionally-promoted polysulfide redox electrochemistry, Chem. Eng. J. 427 (2022).
[71] H. Li, S. Ma, J. Li, F. Liu, H. Zhou, Z. Huang, S. Jiao, Y. Kuang, Altering the reaction mechanism to eliminate the shuttle effect in lithium-sulfur batteries, Energy Storage Mater. 26 (2020) 203–212.